

Generated using the official AMS L^AT_EX template v6.1 two-column layout. This work has been submitted for publication. Copyright in this work may be transferred without further notice, and this version may no longer be accessible.

Surface heating steers planetary-scale ocean circulation

DHRUV BHAGTANI,^a ANDREW McC. HOGG,^a RYAN M. HOLMES,^b NAVID C. CONSTANTINOU,^a

^aResearch School of Earth Sciences & ARC Center of Excellence for Climate Extremes, Australian National University, Canberra, Australia

^bSchool of Geosciences, University of Sydney, Sydney, Australia

ABSTRACT: Gyres are central features of large-scale ocean circulation and are involved in transporting tracers such as heat, nutrients, and carbon-dioxide within and across ocean basins. Traditionally, the gyre circulation is thought to be driven by surface winds and quantified via Sverdrup balance, but it has been proposed that surface buoyancy fluxes may also contribute to gyre forcing. Through a series of eddy-permitting global ocean model simulations with perturbed surface forcing, the relative contribution of wind stress and surface heat flux forcing to the large-scale ocean circulation is investigated, focusing on the subtropical gyres. In addition to gyre strength being linearly proportional to wind stress, it is shown that the gyre circulation is strongly impacted by variations in the surface heat flux (specifically, its meridional gradient) through a rearrangement of the ocean's buoyancy structure. On shorter timescales (\sim decade), the gyre circulation anomalies are proportional to the magnitude of the surface heat flux gradient perturbation, with up to $\sim 0.15 \text{ Sv}$ anomaly induced per W m^{-2} change in the surface heat flux. On timescales longer than a decade, the gyre response to surface buoyancy flux gradient perturbations becomes non-linear as ocean circulation anomalies feed back onto the buoyancy structure induced by the surface buoyancy fluxes. These interactions complicate the development of a buoyancy-driven theory for the gyres to complement the Sverdrup relation. The present study challenges the conventional understanding of the interplay between fundamental drivers of the large-scale ocean circulation.

SIGNIFICANCE STATEMENT: Ocean gyres are large swirling circulation features that redistribute heat across ocean basins. It is commonly believed that surface winds are the sole driver of ocean gyres, but recent literature suggests that other mechanisms could also be influential. Here, we perform a series of numerical simulations in which we artificially change the winds or the heating at the ocean's surface and investigate how each factor independently affects the ocean gyres. We find that gyres are steered by both winds and surface heating, and that the ocean circulation behaves differently to heating on short and long timescales. In addition, the circulation depends on where the heating is applied at the ocean's surface. Through these simulations, we argue that a complete theory explaining the formation of gyres should consider heating at the ocean's surface as a possible driver, in addition to the winds.

1. Introduction

The large-scale ocean circulation derives its energy from a variety of sources including wind stress (Wunsch and Ferrari 2004; Hughes and Wilson 2008; Jamet et al. 2021), tidal forces (Oka and Niwa 2013), and surface and geothermal buoyancy fluxes (Hughes et al. 2009; Hogg and Gayen 2020). Gyres are fundamental elements of the large-scale circulation and play a crucial role in the biogeochemical and hydrological cycles in the ocean by transporting momentum, heat, nutrients and chemicals within and across ocean basins (Webb 2017). In particular, gyres contribute

to global heat transport by transferring heat poleward (Palter 2015; Zhang et al. 2021; Li et al. 2022). Despite their importance in regulating large-scale weather and climate patterns, the interplay between the processes leading to the formation and evolution of ocean gyres are not fully understood.

Traditional oceanographic literature on the drivers of ocean circulation suggest that near-surface horizontal flows are primarily caused by mechanical forcing due to wind stress (Sverdrup 1947) and tidal forces (Wunsch and Ferrari 2004; Oka and Niwa 2013), and the meridional overturning circulation (MOC) is chiefly driven by surface buoyancy fluxes (Stommel and Arons 1959). However, this simplified viewpoint has been amended with time. Recent literature points to a definitive role played by wind stress on the MOC through isopycnal upwelling in the Southern Ocean (Abernathy and Ferreira 2015; Hogg et al. 2017) and bottom-enhanced diapycnal mixing (Stanley and Saenko 2014; Drake et al. 2020). Similarly, buoyancy forcing is thought to exert a significant control on horizontal circulation through the conversion from potential to kinetic energy (Tailleux 2009; Hughes et al. 2009) and control of the stratification in the ocean (Shi et al. 2020), consistent with the fundamental dynamics of rotating horizontal convection (Gayen and Griffiths 2021). In this paper, we aim to evaluate the interplay between wind stress and surface buoyancy forcing in driving various features of the large-scale ocean circulation, with an emphasis on basin-scale ocean gyres.

Considerable progress has been made to elucidate the impact of surface wind stress on ocean gyres (Sverdrup

Corresponding author: D. Bhagtani, dhruv.bhagtani@anu.edu.au

1947; Stommel 1948; Munk 1950; Rhines and Young 1982; Luyten et al. 1983; Pedlosky 1986). Munk (1950) proposed the Sverdrup relation by constructing a relationship between the curl of the wind stress and the depth-integrated meridional geostrophic transport, valid in the ocean interior away from coastlines,

$$V = \frac{\hat{z} \cdot (\nabla \times \boldsymbol{\tau})}{\beta}, \quad (1)$$

where $V = \rho_0 \int v dz$ is the time-mean depth-integrated meridional mass transport with ρ_0 the ocean's reference density, \hat{z} is the unit vector in the vertical, $\boldsymbol{\tau} = \tau_x \hat{x} + \tau_y \hat{y}$ the time-mean horizontal wind stress at the ocean's surface, and $\beta = \partial f / \partial y$ is the meridional gradient of the Coriolis frequency f . The return flow occurs as an intense inertial western boundary flow (see, e.g., Hughes and Cuevas (2001)). The Sverdrup relation (1) describes the dependence of the horizontal structure of barotropic gyres on the wind stress curl, and to date, remains the corner-stone theory of wind-driven gyres.

The Sverdrup relation focuses on understanding the horizontal structure of the vertically-integrated gyre transport. The ventilated thermocline theory, developed by Luyten et al. (1983), made further strides in interpreting the vertical structure of ocean gyres forced by wind stress. They obtained a layer-wise meridional transport for gyres but restricted gyre transport to only ventilated isopycnals; that is, isopycnals outcropping to the surface of the ocean, with non-ventilated isopycnals at rest. However, several studies point to a net re-circulatory transport in the non-ventilated isopycnal layers (Rhines and Young 1982; McDowell et al. 1982) so long as they do not interact with the ocean's surface or topography. Therefore, ocean gyres can be viewed as a combination of ventilation and recirculation regimes, and are controlled by surface wind stress curl.

Wind-driven theories encapsulate gyre circulation to zeroth order, however, observational studies show deviations from the Sverdrup relation. Gray and Riser (2014) examined the validity of Sverdrup dynamics in a point-wise manner using observations from Argo floats (Roemmich et al. 2004) and found that it agrees well with observations in the interior subtropical gyres, with significant deviations in subpolar regions. Colin De Verdière and Ollitrault (2016) obtained a depth-integrated geostrophic transport using Argo data (Ollitrault and Rannou 2013) and World Ocean Atlas 2009 (Locarnini et al. 2010) to estimate a global Sverdrup streamfunction, which was found to underrepresent the subtropical and subpolar gyre strength by a factor of 2. These discrepancies indicate the presence of other processes playing a role in the vorticity balance, such as bottom pressure torques (Hughes and Cuevas 2001), diapycnal mixing (Lavergne et al. 2021), buoyancy forcing (Hogg and Gayen 2020; Liu et al. 2022) and coupling with the meridional overturning (Klockmann et al. 2020;

Berglund et al. 2022). At present, a unified theory encapsulating all the previously stated mechanisms is not available, which limits our understanding of the coupling between these processes, as well as their combined effects on ocean circulation. The present paper makes an attempt to isolate and understand the roles of wind stress and surface buoyancy forcing in shaping the planetary-scale ocean gyres.

Surface buoyancy forcing alters the ocean's density structure through heat and freshwater fluxes (Large and Yeager 2009; Talley et al. 2011). Together with the thermal wind relation,

$$f \frac{\partial \mathbf{u}}{\partial z} = \hat{z} \times \nabla b, \quad (2)$$

where $b(\mathbf{x}, t) = g(1 - \rho(\mathbf{x}, t)/\rho_0)$ is the buoyancy, with g the gravitational acceleration, these density structure changes can be used to understand how changes in surface buoyancy forcing might impact ocean circulation. However, the relationship between surface buoyancy forcing and the horizontal circulation is complicated. For example, variations in mixed layer depth and non-linear feedbacks with the ocean circulation both influence how the surface buoyancy forcing is “felt” within the ocean. The mixed layer ingests a fraction of the surface buoyancy flux, which is reflected in the anomalous ocean's density within the layer. The amount of buoyancy forcing reaching the layers below is thus inversely related to the mixed layer depth, with a deeper mixed layer taking a longer time to relay the excess buoyancy forcing into the subsurface layers (Xie et al. 2010) due to its higher effective heat capacity. Furthermore, the circulation modifies the influence of surface buoyancy forcing on the ocean's buoyancy structure through heat advection (Bryden et al. 1991). Advection acts to alter the buoyancy structure remote from the forcing, which, in view of (2), would also cause anomalies in the ocean circulation in that remote location. In this paper, we evaluate the variability in ocean's stratification over time to better understand the non-linear and non-local connection between the surface buoyancy forcing and the gyres.

Past studies examined the role of surface buoyancy forcing in restructuring ocean gyres. Goldsborough (1933) observed that freshwater fluxes can drive horizontal circulation via induced sea surface height anomalies. Luyten et al. (1985) and Pedlosky (1986) extended the ventilated thermocline theory (Luyten et al. 1983) to include an interfacial mass flux between various isopycnal layers (to represent surface buoyancy forcing), and using a simplified ocean model, demonstrated a geostrophic baroclinic flow induced by the buoyancy flux and steered by wind stress. Colin de Verdière (1989) used a model similar to Cox and Bryan (1984) but coupled the surface buoyancy forcing to wind stress via a bulk formula and concluded

that the former drives a baroclinic mode to significantly recast the horizontal and vertical structure of subtropical gyres. Gjermundsen et al. (2018) instead considered simulations conducted in the absence of any surface momentum inputs and applied buoyancy flux at the ocean's surface through a meridionally varying surface temperature restoring profile. They observed a broad eastward zonal flow as a consequence of the surface buoyancy flux structure and the thermal wind balance as well as a western boundary current. Hogg and Gayen (2020) conducted a series of numerical simulations with a restoring temperature profile and no wind stress in two configurations: a direct numerical simulation in a 3D box domain, and a layered general circulation model in a sector configuration, and found a double (resembling a subtropical and subpolar) gyre in both scenarios. With a multitude of contrasting viewpoints on the processes leading to the formation of gyres, we are motivated to examine further the role of surface buoyancy forcing in driving ocean gyres.

It is worth emphasizing here that ocean gyres do not exist in isolation – they interact with other fundamental aspects of ocean circulation, such as the MOC. The MOC complements gyre circulation in transporting tracers such as heat, chemicals, and nutrients globally between ocean basins. It has been argued that thermohaline forcing is responsible for driving the MOC (Stommel and Arons 1959; Stommel 1961), with gyres being driven by wind stress (Munk 1950). Luyten et al. (1985) contradicted this simplified view by establishing a link between wind stress and heat gain for the North Atlantic subpolar gyre. Yeager and Danabasoglu (2014) and Yeager (2015) used a coupled ocean-sea-ice configuration of the Community Earth System Model with perturbed forcing, and found that most of the decadal variability in both the Atlantic MOC (AMOC) and the North Atlantic subpolar gyre was due to variability in surface buoyancy forcing, while changes in interannual variability were attributed to wind stress anomalies. Modeling studies (Yeager 2015; Larson et al. 2020) identify a direct relationship between the mid-depth overturning cell and the North Atlantic subtropical gyre transport on the basis that the two circulatory features are linked through the northward flowing Gulf Stream. Thus, ocean gyres and the MOC are coupled dynamical features (Klockmann et al. 2020; Berglund et al. 2022), and a thorough analysis of the drivers behind the formation of ocean gyres requires a quantitative understanding of other processes of ocean circulation.

The objectives of the present paper are: (*i*) to quantify how the surface buoyancy forcing affects the structure of ocean gyres, and (*ii*) to understand how wind stress and surface buoyancy fluxes act in concert to drive large-scale ocean circulation. Section 2 outlines the simulation setup and a gyre metric used to analyze the ocean's circulation. Section 3 examines the sensitivity of gyre circulation to

changes in surface wind stress, followed by a brief discussion of the coupling between gyres and other large-scale circulation features in the ocean. Section 4 further investigates the role of surface buoyancy forcing gradients in steering the ocean circulation. In section 5 we look at a uniform warming experiment to illustrate that changes in ocean circulation can also occur in the absence of a meridional gradient in buoyancy forcing anomaly. In section 6, we conclude by emphasizing the connected roles of wind stress and surface buoyancy fluxes in driving ocean circulation, the importance of surface buoyancy forcing in driving ocean gyres, and future directions to advance our understanding of ocean circulation.

2. Models and Methods

a. Flux-forced simulations

Surface buoyancy fluxes in ocean-sea ice general circulation models are usually parameterized using bulk formulae (Large et al. 1994), and are therefore dependent on the model's dynamic sea surface temperature, as well as the externally prescribed atmospheric winds, humidity, air temperature and radiative fluxes. Therefore, any changes in circulation (for example due to changes in wind stress) have the ability to alter the surface buoyancy forcing. To isolate the impacts of wind and surface buoyancy forcing from each other, in this study we construct a series of global simulations where we force the ocean using fluxes at the surface. We call them “flux-forced” simulations. The flux-forced simulations permit us to modify the surface boundary fluxes independently, in that they decouple the wind and surface buoyancy forcing from each other.

Forcing for the flux-forced control experiment is constructed from a 200-year control simulation using ACCESS-OM2-025 (Kiss et al. 2020), a global ocean-sea ice model at 0.25° resolution and 50 vertical layers. ACCESS-OM2-025 is an amalgamation of the Modular Ocean Model v5.1 ocean model (Griffies 2012) and the CICE v5.1.2 (Hunke et al. 2015) sea ice model. We apply a repeat-year atmospheric forcing using the JRA55-do v1.3 reanalysis product (Tsujino et al. 2018) to drive the ACCESS-OM2-025 control simulation. We use the period 1st May 1990 to 30th April 1991 as the repeat year for atmospheric forcing following Stewart et al. (2020). The ACCESS-OM2-025 control experiment is initialized using temperature and salinity data from the World Ocean Atlas 2013 (Locarnini et al. 2013; Zweng et al. 2013), and incorporates the Gent-McWilliams parameterization (Gent and McWilliams 1990) (with a maximum diffusivity of $200 \text{ m}^2 \text{ s}^{-1}$) to complement partially resolved mesoscale eddy fluxes. Vertical mixing is parameterized using a slightly altered K-profile parameterization (Large et al. 1994) (see Appendix). The 200-year control ACCESS-OM2-025 simulation is used to create a climatology of surface boundary fluxes at 3-hourly temporal frequency,

obtained by combining the last 20 years of surface forcing data.

The flux-forced simulations apply the climatology of surface boundary fluxes to a stand-alone implementation of the Modular Ocean Model v5.1 (Griffies 2012). The flux-forced control experiment is initialized from the end of the ACCESS-OM2 control experiment and run for 100 years, after which we branch off a series of flux-forced perturbation simulations with modified surface fluxes. These perturbation experiments are run for another 100 years. Although 100 years is not sufficient for the deep ocean to reach equilibrium, it is enough for the upper and mid-ocean circulation to respond to changes in surface forcing (Saenko 2009).

We conduct three types of sensitivity experiments:

- (i) Perturbations in surface wind stress,
- (ii) Perturbations in surface meridional heat flux gradients, and
- (iii) A ‘uniform warming’ perturbation.

A list of all flux-forced experiments is given in Table 1. Each set of experiments is described below.

We perform wind perturbation experiments by increasing or decreasing the global wind stresses by a multiplicative factor of 0.5 or 1.5 respectively (Table 1).

The construction of surface buoyancy flux gradient perturbation experiments is based on the thermal wind relation (2), which suggests a dependence of the ocean circulation on horizontal density gradients, which in turn could be modified by prescribing a spatially varying buoyancy flux perturbation at the ocean’s surface. Herein, we apply buoyancy flux perturbations by varying the prescribed surface heat fluxes. The largest heat losses in the ocean occur in focused regions over the subtropical western boundary currents (Fig. 1a). The fine-scale spatial structure in the surface heat fluxes differs from the broader patterns of the wind stress forcing, and for that reason, choosing a multiplicative approach for surface buoyancy flux perturbations would enhance this fine-scale structure, which could potentially instigate spurious behavior in ocean circulation. Furthermore, a multiplicative approach would potentially lead to strong convection over the western boundary currents where heat loss in the control is strongest (Fig. 1b). Therefore, for our buoyancy flux gradient perturbations we choose instead to add or subtract a broad surface heat flux pattern (Fig. 1) to the flux-forced control simulation, multiplied by a constant flux amplitude for each experiment (Table 1) to enhance or reduce the meridional buoyancy gradients. We ensure that the global integral of the pattern is zero by adjusting the magnitude of the heat flux in subpolar and polar regions to be double the magnitude of heat flux in subtropical regions (which has twice the area), with zero perturbation in the tropics. To minimize

any spurious behavior in ocean circulation due to the applied buoyancy perturbation, we employ a hyperbolic tangent function ($\tanh[(y - y_0)/\Delta y]$) over the latitude band of $\Delta y = 12.5^\circ$, with y_0 the transition latitude; see Fig. 1b) at the junction between subtropical and subpolar buoyancy anomalies. Buoyancy perturbation experiments for which the mask is multiplied by a positive value have surface heat fluxes that enhance the near-surface meridional buoyancy gradients, and are labeled as “increased buoyancy flux contrast” experiments. Conversely, all experiments where the buoyancy perturbation mask is multiplied by a negative value are labeled as “reduced buoyancy flux contrast” experiments. We were unable to run a -30 W m^{-2} simulation as it became unstable due to unrealistically warm sea surface temperatures at high latitudes.

Finally, we conduct a globally uniform warming experiment, which differs from the surface meridional heat flux gradient perturbation experiments in that we do not externally induce a surface buoyancy gradient in the ocean. However, we still anticipate anomalies in the circulation owing to its non-local and non-linear feedback with the surface buoyancy forcing, and lateral variations in the mixed layer depth.

Our flux-forced control simulation is not fully equilibrated as shown in Fig. 1c, where the mean sea surface temperatures gradually increase with time ($\approx 0.1^\circ \text{C decade}^{-1}$). The systematic increase is due to frazil formation in polar latitudes, which is modeled via an additional heat input. This heat gain is a proxy for heat transferred by a fictional ice model coupled to the flux-forced ocean model, as cold water is converted to ice. Frazil formation in our experiments is not prescribed like the other surface heat fluxes; instead, it depends on ocean temperature and acts to alleviate excessive cooling in polar regions. The dependence of frazil formation on the surface buoyancy forcing limits the magnitude of buoyancy flux perturbation we can apply at the ocean’s surface without the simulation becoming unstable. Moreover, the heat gain due to frazil formation is amplified in increased buoyancy contrast experiments with a stronger heat loss in subpolar and polar regions. This net heat gain is partially mitigated by applying a globally uniform heat loss of 1.28 W m^{-2} to all increased buoyancy flux contrast experiments. The resulting heat flux anomalies due to frazil formation are much smaller than the buoyancy perturbations applied in our sensitivity experiments, and therefore, we do not expect any significant departures in ocean circulation due to this frazil formation induced buoyancy gain.

b. Gyre metrics

Gyre strength is generally defined as the vertically integrated mass transport from surface to bottom. However, this procedure of estimating gyre strength disregards the baroclinic component of gyre strength, which integrates

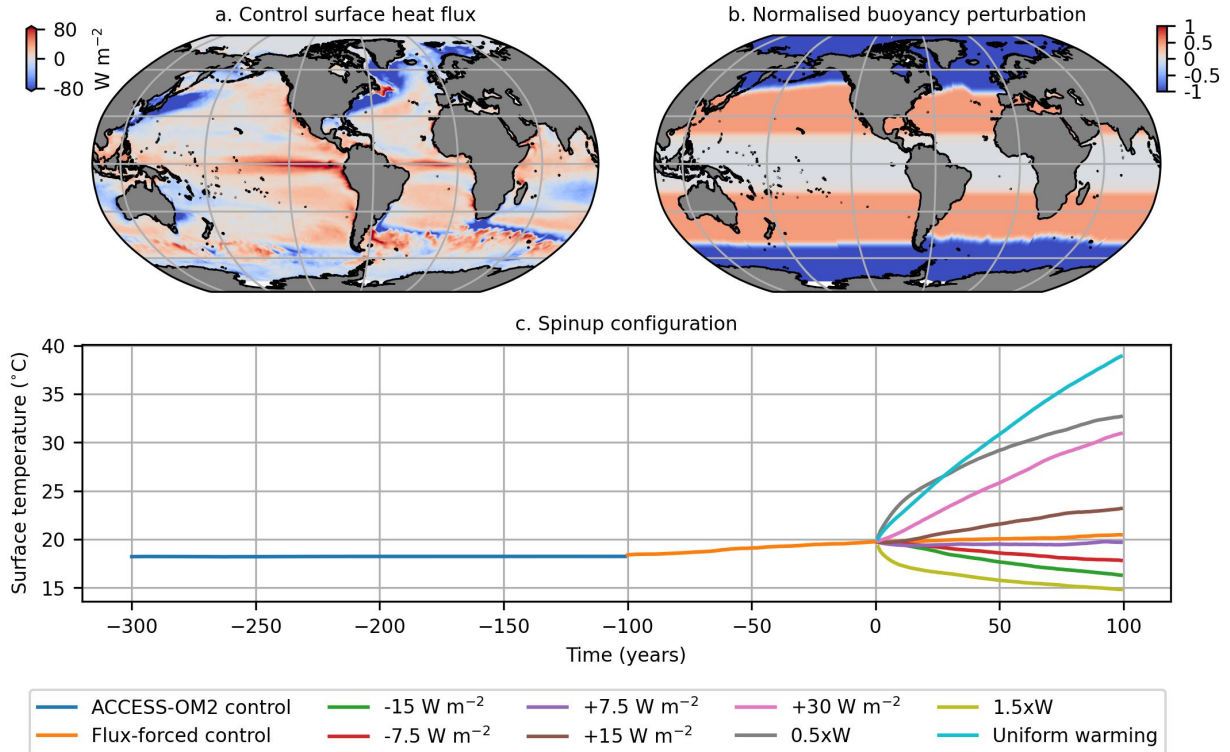


FIG. 1: Model setup for sensitivity experiments. (a) Climatological net surface heating for flux-forced control simulation. (b) Surface buoyancy flux perturbation pattern. This pattern is multiplied by a scale factor and then applied to panel (a) to construct the surface buoyancy flux perturbation experiments. The perturbation pattern is -1.0 in subpolar and polar regions, and $+0.5$ in subtropical regions, with a 1.5 meridional contrast between the two extrema. A hyperbolic tangent function is used to smoothly connect: (i) subtropical and subpolar regions and (ii) subtropics and tropics. (c) Global average surface temperature from each simulation performed in this study, illustrating the model spinup method. Simulation time is referenced with respect to the beginning of the flux-forced perturbation experiments.

TABLE 1: List of experiments. G denotes perturbation applied globally and G-T perturbations that exclude the tropics, defined as the equatorward extent of subtropical gyres in the equilibrated flux-forced control simulation (see Fig. 1b).

Experiment	Wind Factor	Surface Buoyancy Flux Contrast ΔB (W m^{-2})	Region
Control	1	0	G
$0.5 \times W$	0.5	0	G
$1.5 \times W$	1.5	0	G
-15 W m^{-2}	1	-15	G-T
-7.5 W m^{-2}	1	-7.5	G-T
$+7.5 \text{ W m}^{-2}$	1	+7.5	G-T
$+15 \text{ W m}^{-2}$	1	+15	G-T
$+30 \text{ W m}^{-2}$	1	+30	G-T
Uniform warming	1	0, instead <i>spatially uniform</i> +5	G

to zero in depth. To circumvent this issue, we estimate the subtropical gyre strength using an “isopycnal outcropping method”. We integrate the horizontal mass transport

from the surface only to the depth of the densest isopycnal (measured using potential density referenced to 2000 dbar and denoted as σ_{\max}) that outcrops to the ocean’s surface

in a given basin (marked by the red boxes in Fig. 2). For simplicity, we choose $\sigma_{\max} = 1035.8 \text{ kg m}^{-3}$ for all four subtropical gyres in each flux-forced simulation. Then, to arrive at a single scalar estimate of the gyre's strength, we select the 95th percentile (to filter out vigorous inertial re-circulating eddies near the western boundary region) of a 5-year running mean (to filter out transient eddies and seasonal isopycnal outcropping) of the resulting density-integrated horizontal transport streamfunction.

The isopycnal outcropping method captures the baroclinic component of gyres, and is used in all flux-forced simulations to compare the gyre strength. However, it suffers from two limitations:

1. Surface buoyancy perturbations could restructure the ocean's stratification, which may alter the isopycnal regime occupied by the gyres. These changes are not well-represented in the isopycnal outcropping method, since the method integrates the entire circulation from the surface to $\sigma_{\max} = 1035.8 \text{ kg m}^{-3}$. We use a deep isopycnal for σ_{\max} to ensure we fully capture the subtropical gyres. In doing so, we may record a portion of abyssal circulation, which is usually much weaker than near-surface circulation. Thus, this method characterizes the subtropical gyre strength.
2. Computing the streamfunction requires that the flow is divergence-free, which is not guaranteed due to the possibility of a net transport across the σ_{\max} isopycnal. However, in the ocean's interior, flow across isopycnals is much more restricted compared to flow along isopycnals (see, e.g., Abernathay et al. 2022) and, therefore, our streamfunction calculations are correct to leading order.

3. Wind stress perturbation experiments

In this section, we investigate two perturbation experiments wherein we change the magnitude of wind stress by 0.5 and 1.5 times the control experiment, which alters the time-mean vorticity input due to the wind stress curl by the same factor. We analyze short-term and long-term variations in the subtropical gyre transport for Atlantic and Pacific oceans for both hemispheres, along with a brief discussion of their coupling with the Meridional Overturning Circulation (MOC) and Antarctic Circumpolar Current (ACC). Since our flux-forced experiments do not incorporate sea-ice dynamics, changes in Weddell and Ross gyres are not reported in the paper, as sea-ice can significantly alter gyre dynamics in polar regions.

The dashed lines in the time series in Fig. 2 show the expected transport as predicted by the Sverdrup linear scaling of the average gyre transport in the control experiment for the last 100 years of the simulation. Subtropical gyres follow Sverdrup scaling to a large extent, consistent with

the ventilated thermocline theory (Luyten et al. 1983); deviations are observed in the North Atlantic subtropical gyre in both wind perturbation simulations, and in the 0.5×W simulation in the North Pacific subtropical gyre.

The gyre strengths adjust quickly to changes in wind forcing (solid curves in the time series in Fig. 2), which is likely due to a quick adjustment of the western boundary current by barotropic Rossby waves (Veronis and Stommel 1956; Anderson and Gill 1975). Subsequent smaller changes in gyre transports may be attributed to baroclinic Rossby waves, which propagate slowly and have a smaller effect on the gyre circulation (Anderson and Gill 1975). The time series also show that after the initial response, gyres in the Pacific Ocean are more stable than in the Atlantic Ocean.

Next, we analyze the impact of the perturbations in wind stress forcing on other large scale flow metrics, starting with the AMOC. For the first 10 years, the AMOC strength is inversely related to the wind stress magnitude (Fig. 3a), which is likely linked to a change in northward Gulf Stream barotropic transport, part of which lies within the AMOC (evaluated between $\sigma_2 \in [1035.5, 1038] \text{ kg m}^{-3}$ density classes, which captures the bulk of the overturning circulation). Similar results have been reported by Hazeleger and Drijfhout (2006) and Yang et al. (2016). After the initial transient response, we observe a slight decline in AMOC strength for the 0.5×W experiment compared with the control, consistent with previous studies (e.g. Lohmann et al. 2021). However, we also observe a reduction in the AMOC in the 1.5×W experiment in the first 60 years, while a gradual increase to about 10% compared with the control experiment is observed in the next 40 years. These positive anomalies in AMOC in the last 40 years with increased wind stress could be associated with eddy compensation in the Southern Ocean (Morrison and Hogg 2013), or other non-linear feedback in the ocean circulation.

We observe only slight ($\approx 4\%$) changes in the ACC transport in both 0.5×W and 1.5×W simulations compared to the control (Fig. 3b), which is consistent with several numerical studies that the ACC is weakly sensitive to the strength of the wind stress due to a process known as eddy saturation (Munday et al. 2013; Marshall et al. 2017; Constantinou and Hogg 2019). However, the validity of ACC transport (especially the inconsistent reduction in the 1.5×W simulation) may be questioned on the basis that the control flux-forced experiment is not equilibrated, and declines steadily ($\approx 9\%$) during the same time period.

We observe a near-linear relationship between the globally integrated kinetic energy (Fig. 3c) and wind stress magnitude. Winds supply energy to the ocean through generation of eddies and enhanced circulation, which leads to an increase in the global kinetic energy (Wunsch and Ferrari 2004). We discern that the change in kinetic energy due to wind stress is partially due to a change in the gyre

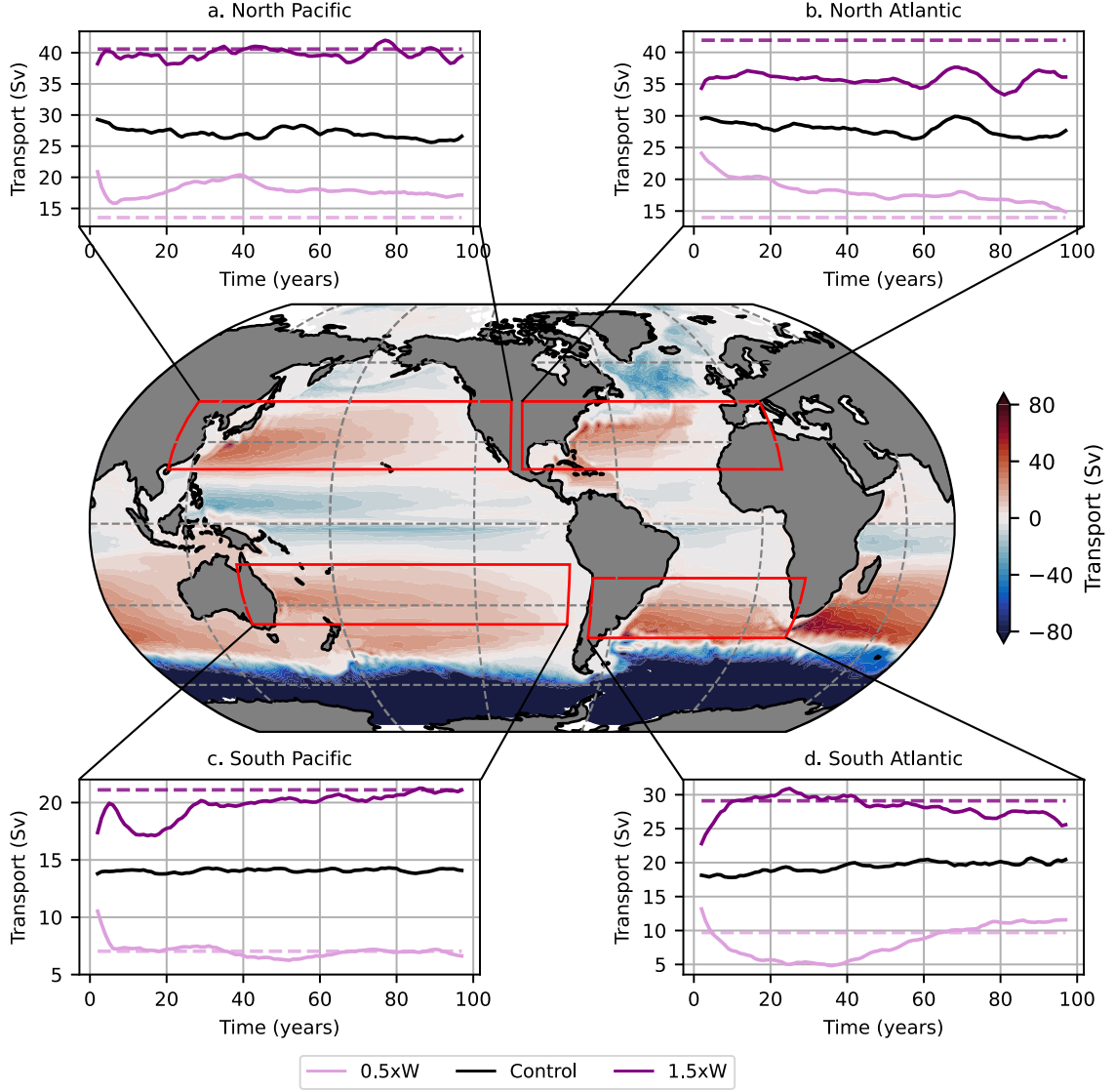


FIG. 2: The barotropic streamfunction averaged over the last 15 years of the flux-forced control experiment. The streamfunction is multiplied with $\text{sign}(f)$. The subpanels show time series of gyre strength for the control (black), $0.5 \times W$ (pink), and $1.5 \times W$ (purple) experiments in the (a) North Pacific subtropical gyre, (b) North Atlantic subtropical gyre, (c) South Pacific subtropical gyre, and (d) South Atlantic subtropical gyre. An equal y-axis spacing is used on the y-axis to facilitate comparison between the different gyres. Red boxes show the extent of each basin used to estimate the 95th percentile subtropical gyre strength using the isopycnal outcropping method. Dashed lines show the gyre transport predictions based on Sverdrup linear scaling, i.e., the time-mean gyre strength in the control multiplied by the wind perturbation factor.

circulation (Fig. 2) as well as mesoscale eddies, and only weakly related to the MOC and ACC (Fig. 3). A complete energy budget calculation is not presented here, as it is beyond the scope of the study.

4. Surface buoyancy flux contrast perturbation experiments

a. Reduced surface buoyancy flux contrast experiments

In the previous section, we analyzed the effects of wind stress on the large-scale circulation. In this section, we discuss two sensitivity experiments wherein we reduce the

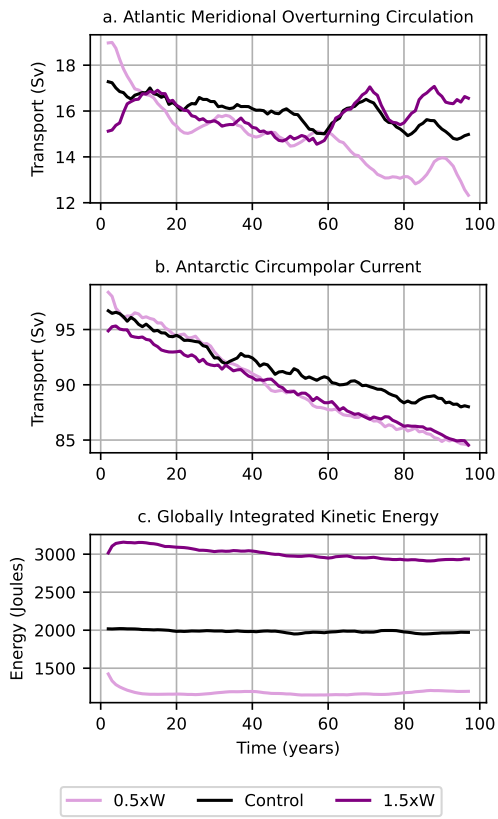


FIG. 3: Monthly-mean time-series circulation metrics for the wind perturbation flux-forced simulations: $0.5 \times W$ (pink), control (black) and $1.5 \times W$ (purple) after a 5-year rolling mean was applied. (a) Atlantic meridional overturning circulation: integrated meridional transport for $\sigma_2 \in [1035.5, 1038.0] \text{ kg m}^{-3}$ at 26°N for longitudes between 103°W and 5°W . (b) Antarctic Circumpolar Current transport through the Drake Passage. (c) Globally integrated kinetic energy.

intergyre surface meridional buoyancy difference at the poleward zonal peripheries of subtropical gyres by 7.5 and 15 W m^{-2} . The buoyancy contrast perturbation is expected to cause variations in horizontal density gradients: from the thermal wind relation (2), these variations could lead to anomalies in the ocean circulation.

We analyze short (< 1 decade) and long (> 1 decade) time responses of the four subtropical gyres to delineate the linear and non-linear behavior of the ocean circulation due to the surface buoyancy flux gradient anomalies. The subtropical gyres, with the exception of the South Pacific gyre, initially reduce compared with the control simulation (Fig. 4). This first-decade reduction is approximately linear with respect to the magnitude of the surface buoyancy flux gradient anomaly, as shown by the red bars in Figs. 4a-

c for the -7.5 W m^{-2} and -15 W m^{-2} experiments. The relaxation in gyre strength is consistent with the thermal wind relation (2): reduction in buoyancy gradients acts to reduce horizontal flow. The bar graphs alongside the gyre strength time series in Fig. 4 reveal that the Atlantic subtropical gyres initially react 2 to 4 times more strongly (measured by the percentage change in the gyre transport) to changes in surface heat fluxes than the Pacific subtropical gyres. However, with time, the Pacific gyres display a greater change than the Atlantic gyres. The time series reveal that the Atlantic gyres are more susceptible to a reduction in surface meridional buoyancy forcing contrast than the Pacific Ocean on short timescales.

Figures 5 and 6 highlight spatial and temporal variations in the ocean's density structure due to the applied heat flux anomaly. Focusing on the -7.5 W m^{-2} simulation, Figs. 5a and 6a highlight minor stratification anomalies in the first 7 years of the simulation period, with the subtropical Atlantic Ocean demonstrating slightly larger meridional buoyancy gradient anomalies than the subtropical Pacific Ocean. These gradients are consistent with stronger circulation anomalies (through (2)) in the two Atlantic subtropical gyres in the initial stages of the simulation.

In addition to the gyre circulation being linear with respect to the magnitude of the surface buoyancy flux gradient perturbation in the first decade, anomalies in the ocean's buoyancy structure develop linearly with time for the -7.5 W m^{-2} simulation. As an example, the potential density latitude-depth transect for the -7.5 W m^{-2} simulation at the end of 95 years (Figs. 5c) and 6c) is quite similar to the potential density transect for -15 W m^{-2} simulation at the end of 50 years (Figs. 5e and 6e).

The manifestation of surface buoyancy fluxes on the density structure of the ocean, especially on longer time scales, is not always linear, which may lead to a complex circulatory response. Unlike the -7.5 W m^{-2} simulation, Figs. 5d-f and 6d-f suggest that the anomalies in the Atlantic and Pacific Ocean's density structure in the -15 W m^{-2} simulation evolve non-linearly with time in the latter stages of the simulation period due to heat advection by the circulation. Comparing Fig. 5e and Fig. 5f, we notice an increase in potential density in the upper ocean subtropical region in year 95, which is overshadowed by a relatively stronger (to year 50) potential density increase in the subpolar region. The overall effect is a relative (to year 50) increase in meridional density gradients, and therefore, spin up of the northern region of the subtropical gyre in the -15 W m^{-2} simulation by $\approx 18\%$ in the last 20 years of the simulation (Fig. 4a). In summary, surface buoyancy forcing anomalies alter the density structure of the mixed layer and gradually infiltrate to deeper layers. However, this downward infiltration is continuously modified by the ocean circulation through heat redistribution, leading to a

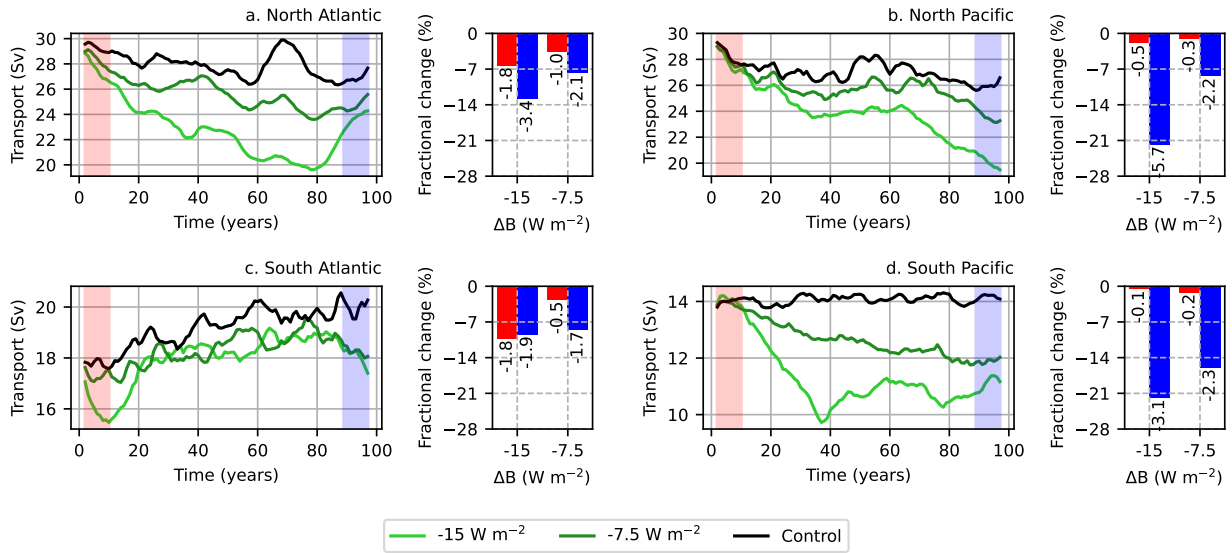


FIG. 4: Comparison of subtropical gyre strength for the reduced surface buoyancy flux contrast experiments. For each gyre, the left panel shows the time series for $-15\ W\ m^{-2}$ (dark green), $-7.5\ W\ m^{-2}$ (light green), and control (black) simulations, and the right panel shows the fractional change in gyre strength with respect to control for the first 10 (red) and last 10 (blue) years of the simulation. Values on each bar depict the absolute change in gyre strength (in Sv) relative to the control.

non-linear evolution of the density structure, and hence the gyre circulation on longer timescales.

In these experiments we observe a weakening of the AMOC with time (Fig. 7a), as a reduction in the surface buoyancy flux gradients causes the subpolar and polar regions to experience a stronger stratification. Stronger stratification suppresses deep water formation in the North Atlantic, which is a major source of the AMOC (Toggweiler and Samuels 1995; Marshall and Speer 2012). The AMOC steadily reduces in the first 60 years of the reduced buoyancy contrast simulations, after which it begins to recover in the $-15\ W\ m^{-2}$ simulation, as opposed to the $-7.5\ W\ m^{-2}$ where it continues to slow down. Moreover, we observe a temporal correlation between the North Atlantic subtropical gyre strength and the AMOC (Figs. 4a and 7a).

There is a nominal ($\approx 2.5\%$) reduction in the circumpolar transport for both $-7.5\ W\ m^{-2}$ and $-15\ W\ m^{-2}$ experiments at the end of 100 years (Fig. 7b). Several competing factors such as reduced meridional buoyancy gradients over the ACC latitude band (Hogg 2010), deepening and shoaling of the thermocline respectively over the northern and southern regions of the ACC, variations in lateral mixing (Ragen et al. 2020), and alterations to the Antarctic bottom water production (Morrison and Hogg 2013) could influence the ACC strength – a thorough analysis is beyond the scope of this study.

Finally, we briefly discuss the changes in ocean circulation due to surface buoyancy forcing anomalies from an energetics perspective. In addition to anomalies observed in the large-scale circulatory features (Figs. 4 and 7a-b), the variations in globally integrated kinetic energy (Fig. 7d) supplement our understanding that surface buoyancy forcing is an important mechanism in steering the ocean circulation. A reduction in surface buoyancy flux gradients inhibits the production of available potential energy, which reduces the conversion from available potential energy to kinetic energy.

b. Increased surface buoyancy flux contrast experiments

In the previous subsection, we considered the short-term and long-term ramifications of reducing surface buoyancy flux gradients on the ocean circulation. A natural follow-up question is: How would the circulation respond to an increase in meridional surface buoyancy flux gradients? Here, we analyze two surface buoyancy perturbation experiments where we increase the meridional surface heat contrast by $+7.5\ W\ m^{-2}$ and $+15\ W\ m^{-2}$ at the latitude of western boundary separation for subtropical gyres using the heat flux perturbation map in Fig. 1b.

Similar to the reduced surface buoyancy flux contrast experiments, the anomalies in the Atlantic Ocean in the increased surface buoyancy flux contrast experiments are induced more quickly than in the Pacific (compare the red bar

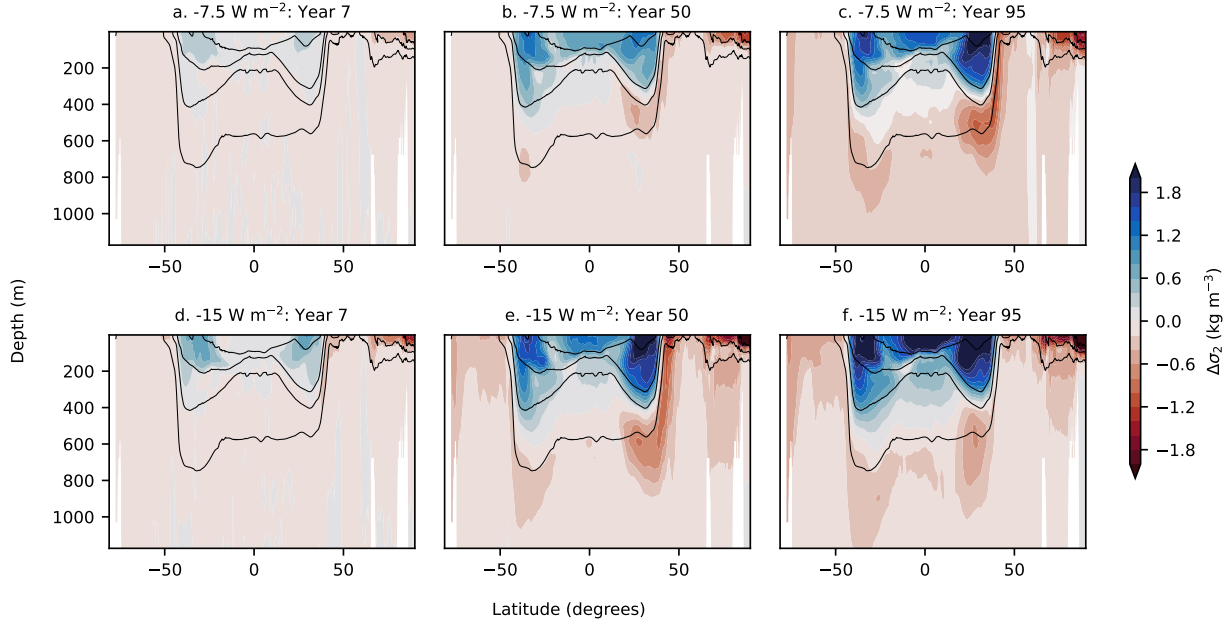


FIG. 5: Potential density (σ_2) anomalies for a longitudinal slice of the upper Atlantic Ocean in the -7.5 W m^{-2} (top row) and -15 W m^{-2} (bottom row) experiments for year 7 (left column), year 50 (middle column) and year 95 (right column), obtained by averaging between 60°W and 30°W for all latitudes. Blue indicates increase in potential density, associated with cooling and/or salinification, whereas red indicates decrease in potential density, associated with heating and/or freshening.

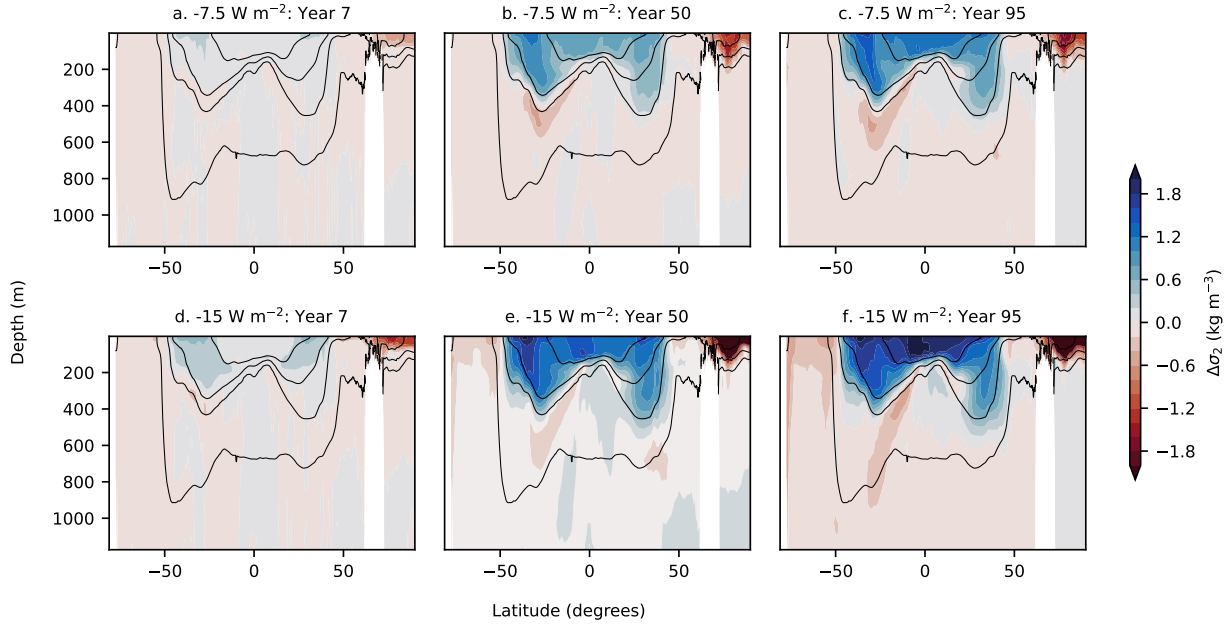


FIG. 6: Potential density (σ_2) anomalies for a longitudinal slice of the upper Pacific Ocean in the -7.5 W m^{-2} (top row) and -15 W m^{-2} (bottom row) experiments for year 7 (left column), year 50 (middle column) and year 95 (right column), obtained by averaging between 220°W and 140°W for all latitudes. Blue indicates increase in potential density, associated with cooling and/or salinification, whereas red indicates decrease in potential density, associated with heating and/or freshening.

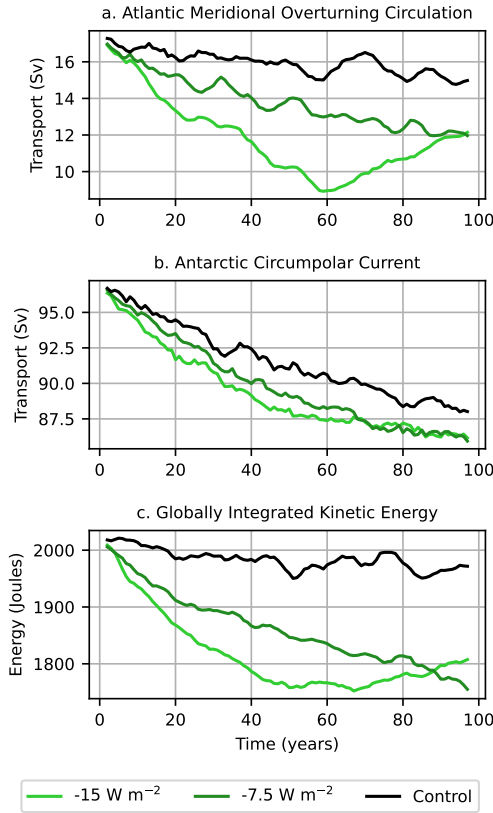


FIG. 7: Circulation metrics for the reduced surface buoyancy flux contrast simulations: -15 W m^{-2} (light green), -7.5 W m^{-2} (dark green), and control (black) after a 5-year rolling mean was applied. (a) Atlantic meridional overturning circulation: integrated meridional transport for $\sigma_2 \in [1035.5, 1038.0] \text{ kg m}^{-3}$ at 26°N for longitudes between 103°W and 5°W . (b) Antarctic Circumpolar Current transport through the Drake Passage. (c) Globally integrated kinetic energy.

graphs in Fig. 8), with the Atlantic gyres in the $+15 \text{ W m}^{-2}$ simulation intensifying by $\approx 20\%$ after 15 years. A linear regression model of the form:

$$\Delta\psi = m\Delta B, \quad (3)$$

is applied, using outputs from the first decade of both the reduced and increased surface buoyancy flux contrast experiments. In this equation, $\Delta\psi$ is the change in gyre circulation, and $m = \Delta\psi/\Delta B$ represents the variation in circulation due to the surface buoyancy contrast ΔB . The regression model predicts a strong linear behavior with reference to the applied surface buoyancy flux contrast for the Atlantic and North Pacific subtropical gyres (inferred from the high R^2 scores in Table 2). Variations in the South

Pacific subtropical gyre due to an applied surface buoyancy contrast in the first 10 years is negligible (Table 2).

On longer timescales, the regression model (3) performs poorly, as the relationship between gyre circulation and anomalous surface buoyancy flux contrast becomes nonlinear with time. This is accompanied by an oscillatory behavior in the gyre strength, as can be observed in the time series in Fig. 8. Although the North Atlantic gyre strength time series shows high variability, the circulation estimates for both $+7.5 \text{ W m}^{-2}$ and $+15 \text{ W m}^{-2}$ simulations are generally greater than the control. The North Pacific subtropical gyre strength anomalies monotonically increase with time for the $+15 \text{ W m}^{-2}$ simulation (Fig. 8b), but show no temporal relation for the $+7.5 \text{ W m}^{-2}$ simulation. The South Atlantic subtropical gyre strength is enhanced in the first decade of the simulations (Fig. 8c), followed by a plateauing for about 20–25 years. The reduction in the South Atlantic subtropical gyre strength in the last 50 years can be attributed to an inaccurate estimate of the circulation: integrating meridional transport for all isopycnals having $\sigma_2 \leq 1035.8 \text{ kg m}^{-3}$ captures a part of the mid-depth overturning circulation. The South Pacific subtropical gyre strength anomalies are minimal for both $+7.5 \text{ W m}^{-2}$ and $+15 \text{ W m}^{-2}$ simulations in the first decade, but grow with time, with the gyre strength in the $+15 \text{ W m}^{-2}$ simulation fluctuating around the control. In conclusion, an oscillatory response is present in all four subtropical gyres, suggesting that there is a complicated feedback between ocean circulation and surface buoyancy forcing.

TABLE 2: Linear regression model (8) for the subtropical gyre perturbations over the first 10 years. R^2 score indicates the extent of gyre variability due to buoyancy forcing that is captured by the linear regression model.

Gyre basin	$m (\text{Sv m}^2 \text{W}^{-1})$	R^2 score
North Atlantic	0.15	0.99
South Atlantic	0.10	0.98
North Pacific	0.02	0.91
South Pacific	0.00	-0.65

The North Atlantic subtropical gyre shows an oscillatory response in terms of strength (Fig. 8a) as well as the western boundary separation latitude (Fig. 9a). The contraction of the northern extent of the subtropical gyre is accompanied by a shoaling and southward expansion of the cyclonic North Atlantic subpolar gyre (compare green contours in Figs. 9c and 9d). The shoaled subpolar gyre carries colder water to the subtropical regions in the near-surface layers, which sits above the less dense subtropical gyre. The unstable vertical structure leads to convection in the northern half of the western boundary region, resulting

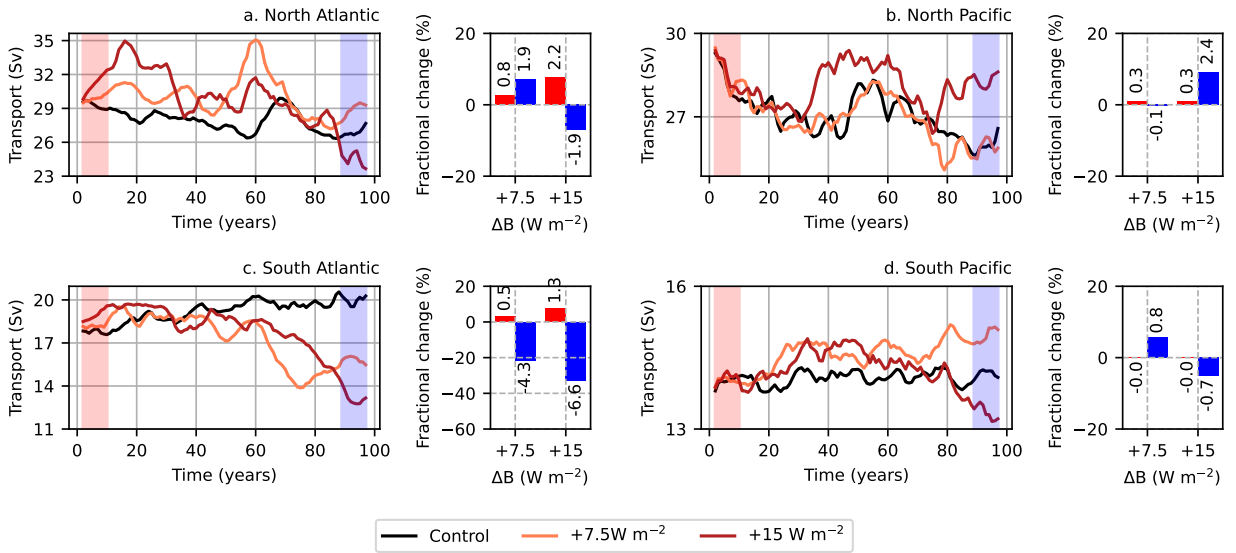


FIG. 8: Comparison of subtropical gyre strength for the increased surface buoyancy flux contrast experiments. For each gyre, the left panel shows the time series for control (black), $+7.5 \text{ W m}^{-2}$ (orange), and $+15 \text{ W m}^{-2}$ (red) simulations, and the right panel shows the fractional change in gyre strength with respect to control for the first 10 (red) and last 10 (blue) years of the simulation. Values on each bar depict the absolute change in gyre strength (in Sv) relative to the control.

in excessively deep mixing layers during that time period (Fig. 9b).

The onset of convection in the North Atlantic basin is associated with the development of an oscillating abyssal anticyclonic gyre below 4000m (Fig. 9e and Fig. 9f). The strength of the abyssal gyre correlates well with the mixing layer depth (Fig. 9b), which in turn is induced by convection in the western boundary of the subtropical gyre. The formation of the abyssal gyre could be explained by two hypotheses: (i) Excessively deep mixing layers due to convection could relay vorticity input due to the surface wind stress directly to the abyssal circulation, or (ii) the southward extension of cyclonic subpolar gyre at the surface could baroclinically stimulate an anti-cyclonic circulation in the deeper layers. A complete analysis of the processes leading to the formation of the abyssal gyre is outside the scope of this study.

In the reduced buoyancy contrast experiments, the density anomalies for the -7.5 W m^{-2} experiment at the end of 100 years closely match with the -15 W m^{-2} simulation at the end of 50 years, suggesting that small reductions in surface buoyancy flux gradients are manifested linearly in the ocean's buoyancy structure. However, this is not true for the positive buoyancy flux anomaly experiments (compare the Atlantic basin in Figs. 10c and 10e, and the Pacific basin in Figs. 11c and 11e). Likewise, we observe a non-linear evolution of the ocean's buoyancy structure in the Atlantic and Pacific basins for the $+30 \text{ W m}^{-2}$ simulation (not presented here).

The AMOC in the increased surface buoyancy flux contrast simulations initially spins up with time, followed by an oscillatory behavior (Fig. 12a). The time taken to display this oscillatory behavior is inversely related to the magnitude of the surface buoyancy flux gradient anomaly. The oscillation of the North Atlantic subtropical gyre strength (Fig. 8a) is similar to that of the AMOC, suggesting a direct relationship between the two. Increased cooling in subpolar regions stimulates the production of NADW, which may cause an acceleration of the mid-depth circulation (Morrison et al. 2011).

The reduced buoyancy flux contrast experiments revealed a weak dependence of circum polar transport on meridional surface buoyancy gradients (Fig. 7c), with temporal variability within experiments being stronger than the anomalies. However, increasing the latitudinal surface buoyancy contrast produces a robust increase in the ACC (Fig. 12b), in agreement with Hogg (2010) and Morrison and Hogg (2013). An increase in the surface buoyancy flux gradients also promotes the conversion of available potential energy to kinetic energy (Fig. 12c), consistent with Tailleux (2009).

5. Uniform warming perturbation experiment

In the previous section, we showed that variations in surface heat fluxes, with opposite signed anomalies applied over subpolar and subtropical regions, can produce anomalies in the ocean circulation. In this section we ask;

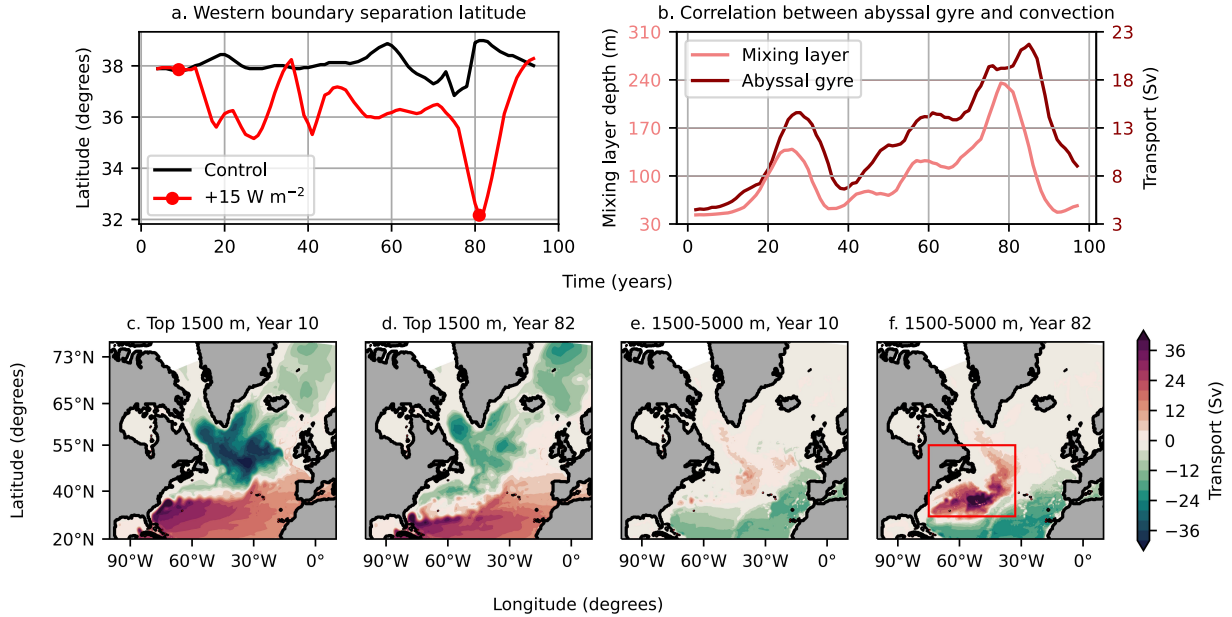


FIG. 9: (a) Western boundary separation latitude of the North Atlantic subtropical gyre for the control (black) and $+15 \text{ W m}^{-2}$ (red) simulations. (b) Temporal correlation between mixing layer depth (light red) and strength of the abyssal gyre (dark red) for $+15 \text{ W m}^{-2}$ simulation. The mixing layer depth is estimated by spatially averaging over the red box in panel (f). The abyssal circulation is measured by taking the 95th percentile of all density classes lying below 3000 m in red box in panel (f). (c)-(f) Streamfunction of the North Atlantic basin for the $+15 \text{ W m}^{-2}$ simulation. Compare the emergence of abyssal gyre (red box in panel (f)) with the beginning of the simulation (panels e), when the entire anticyclonic circulation is confined in the upper 1500 m of the basin. The western boundary separation latitude time series in panel (a) denotes the times (see red dots in panel (a)) that correspond to these streamfunctions.

is the same true if the surface heat flux anomalies are globally uniform? We expect changes in the ocean circulation due to a spatially uniform surface heat flux due to several processes. Firstly, lateral variations in mixed layer depth imply that buoyancy anomalies induced by the uniform heating will be non-uniform. In addition, changes in circulation continuously alter the buoyancy structure of the ocean through advection. To understand the combined effects of mixed layer depth variations and advective feedbacks on the ocean circulation, we analyze a uniform warming experiment, where a globally constant heat flux of $+5 \text{ W m}^{-2}$ is applied at the ocean's surface.

Changes in the strength of each gyre do occur under the uniform warming perturbation (Fig. 13a-c). Focusing first on the North Pacific basin (Fig. 13b), we observe $\sim 22\%$ intensification of the subtropical gyre, consistent with the results of Sakamoto et al. (2005) and Chen et al. (2019). This increase could be attributed to spatial variations in mixed layer depth near the western boundary region. The mixed layer traps the excess heat received from the ocean's surface and distributes only a fraction of this heat to the layer

below. Furthermore, a deeper mixed layer has a higher heat capacity due to its ability to store more heat. Deep mixed layers at the western boundary of the North Pacific subtropical gyre moderately shield the region from developing stratification. Conversely, shallower mixed layers to the east of the western boundary lead to more stratification in that region. The spatially uneven growth of stratification in the subtropical gyre strengthens zonal buoyancy gradients near the western boundary region, which in view of the thermal wind relation, intensifies the meridional gyre flow.

We record a strong ($\sim 50\%$) intensification of the South Atlantic subtropical gyre (Fig. 13c) due to a similar laterally varying mixed layer depth as observed in the North Pacific basin, which augments the zonal buoyancy gradients near the western boundary in response to surface heating. Finally, the South Pacific gyre anomalies show minor oscillations (with an amplitude of $\sim 1.5 \text{ Sv}$) due to uniform surface heating (not shown).

We observe positive anomalies in the North Atlantic subtropical gyre strength for the first 20 years of the uni-

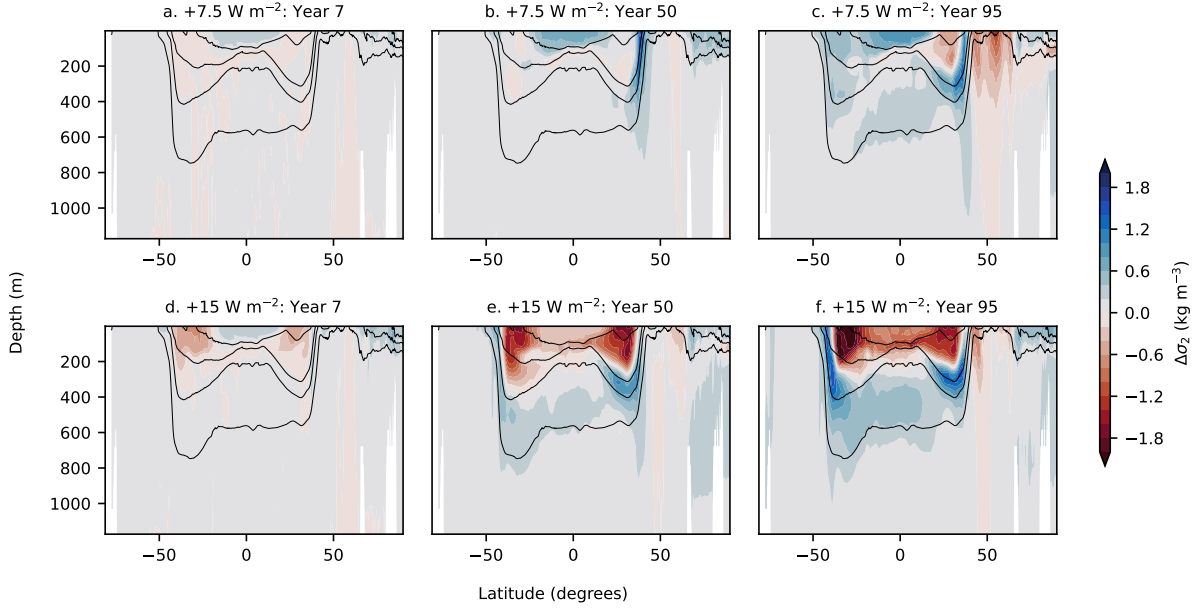


FIG. 10: Potential density (σ_2) anomalies for a longitudinal slice of the upper Atlantic Ocean for $+7.5 \text{ W m}^{-2}$ (top row) and $+15 \text{ W m}^{-2}$ (bottom row) simulation for year 7 (left column), year 50 (middle column) and year 95 (right column), obtained by averaging between 60°W and 30°W for all latitudes. Blue indicates increase in potential density, associated with cooling, whereas red indicates decrease in potential density, associated with heating.

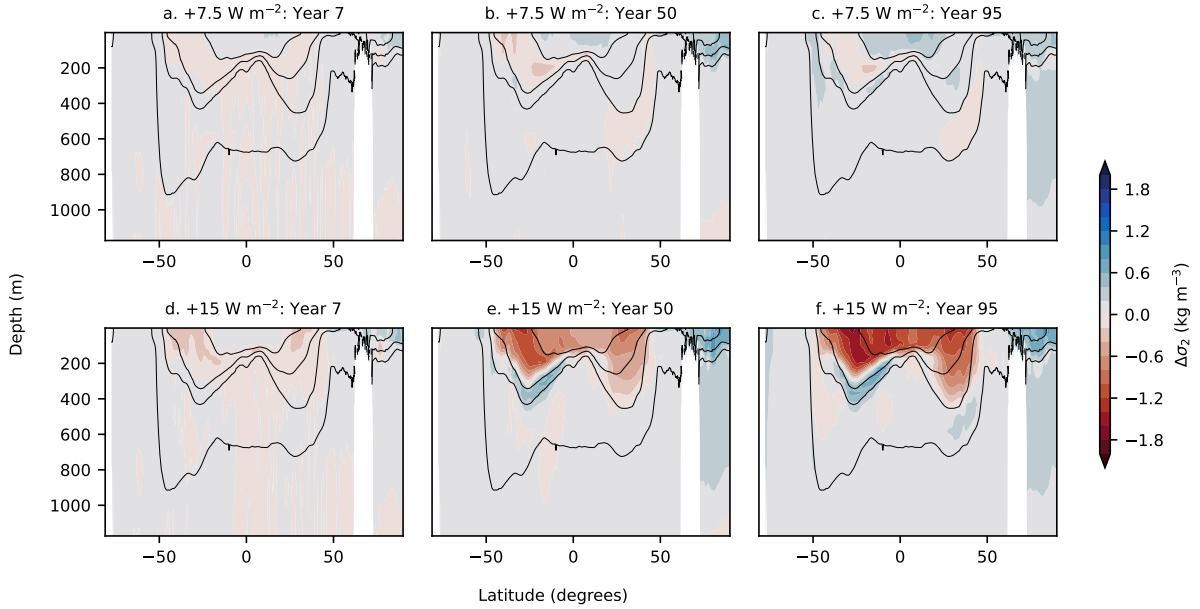


FIG. 11: Potential density (σ_2) anomalies for a longitudinal slice of the upper Pacific Ocean for $+7.5 \text{ W m}^{-2}$ (top row) and $+15 \text{ W m}^{-2}$ (bottom row) simulation for year 7 (left column), year 50 (middle column) and year 95 (right column), obtained by averaging between 220°W and 140°W for all latitudes. Blue indicates increase in potential density, associated with cooling, whereas red indicates decrease in potential density, associated with heating.

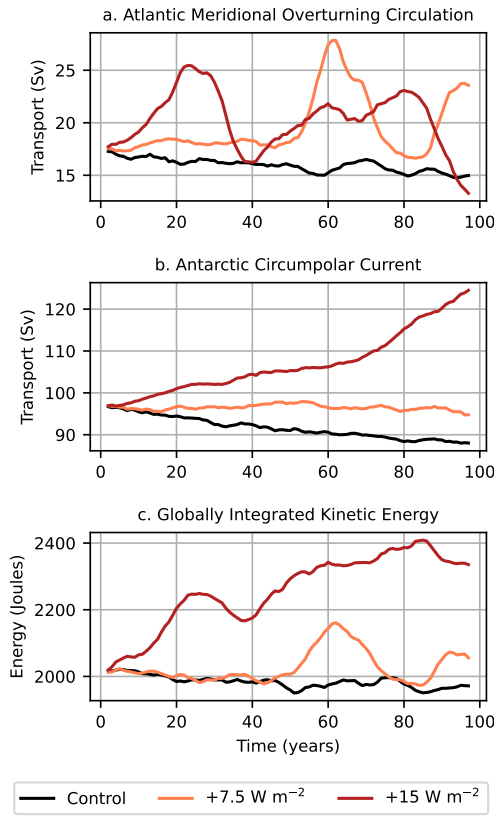


FIG. 12: Monthly-mean time-series circulation metrics for the wind perturbation flux-forced simulations: control (black), $+7.5 \text{ W m}^{-2}$ (orange), and $+15 \text{ W m}^{-2}$ (red) after a 5-year rolling mean was applied. (a) Atlantic meridional overturning circulation: integrated meridional transport for $\sigma_2 \in [1035.5, 1038.0] \text{ kg m}^{-3}$ at 26°N for longitudes between 103°W and 5°W . (b) Antarctic Circumpolar Current transport through the Drake Passage. (c) Globally integrated kinetic energy.

form warming simulation due to differing heat capacities of mixed layer near the Gulf Stream (Fig. 13a). However, the initial spin-up is followed by a systematic slowdown over the next 75 years. Several modeling studies have reported a correlation between the North Atlantic subtropical gyre strength and the AMOC (Yeager 2015; Larson et al. 2020), and we observe a reduction in the AMOC over the same time period (Fig. 13d). This reduction is explained by two processes: (i) the first 20 years of increased gyre strength transports a larger volume of warm water through the Gulf Stream from tropical and subtropical latitudes to the subpolar regions, and (ii) the uniform warming applied at the ocean's surface promotes the generation of lighter waters in the subpolar regions at the ocean's surface. These two processes limit North Atlantic deep water formation,

causing an AMOC slowdown (Lohmann et al. 2008; Cheng et al. 2013).

There is an intensification of the circumpolar transport (Fig. 13e), which could be linked to increased meridional buoyancy gradients due to uneven ingestion of surface buoyancy flux into deeper layers. These irregularities are caused by spatial variations in the mixed layer depth across the latitudinal band of the ACC.

Finally, the globally integrated kinetic energy increases by almost 50% over the full experiment (Fig. 13f). We can ascribe the resulting kinetic energy increase to mean (for example, gyres, ACC) flows as well as mesoscale eddies, and is consistent with the energy conversion argument put forth by Tailleux (2009) that surface buoyancy forcing could induce kinetic energy in the system through a conversion from available potential energy.

6. Summary and Discussion

In this study, we conducted a series of perturbed forcing simulations using a partially eddy-resolving ocean model (at a 0.25° lateral resolution) to understand the importance of wind stress and surface buoyancy forcing in steering planetary-scale ocean circulation. These perturbation experiments (listed in Table 1) are forced for 100 years each using surface boundary fluxes (and are thus called “flux-forced simulations”) to separate the contribution of winds and surface buoyancy in driving the circulation, and are classified into three categories: (i) wind perturbation experiments, (ii) surface buoyancy flux contrast perturbations, and (iii) a spatially uniform warming perturbation.

The flux-forced simulations illustrate that both wind stress (Fig. 2) and surface buoyancy forcing (Figs. 4, 8, and 13a-c) are crucial in shaping the planetary-scale subtropical gyres. We find that perturbations in surface buoyancy flux gradients modify the ocean’s buoyancy structure (Fig. 5, 6, 10, and 11), and thus the circulation through the thermal wind relation (2). In addition, anomalies in horizontal buoyancy gradients (and hence, the circulation (Fig. 13)) could also be induced using a spatially uniform surface heat flux due to lateral differences in mixed layer depth and heat advection by the circulation.

The anomalous horizontal density gradients are proportional to the surface buoyancy flux gradient perturbations on short (< 1 decade) timescales (compare Figs. 5a and d; Figs. 6a and d; Figs. 10a and d; Figs. 11a and d). Through the thermal wind relation (2), we diagnose a linear relationship ($R^2 > 0.9$ in Table 2) between the anomalous gyre circulation and the magnitude of the surface buoyancy flux gradient perturbation on short timescales. Over this period, the Atlantic gyres are observed to be 2-4 times more susceptible to changes in surface buoyancy flux gradients than the Pacific gyres, with as much as a 0.15 Sv anomaly per W m^{-2} change in the subtropical/subpolar surface heat flux in the North Atlantic subtropical gyre.

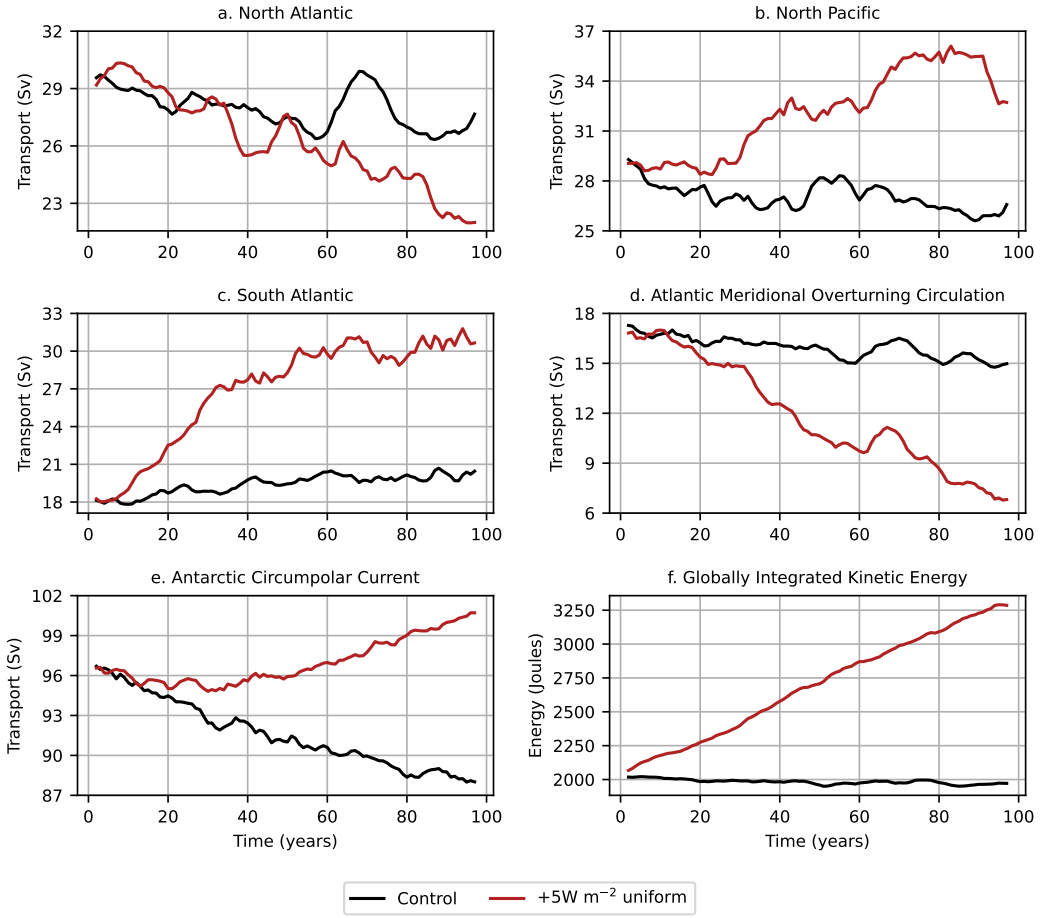


FIG. 13: (a)-(c) Comparison of subtropical gyre strength time series for control (black) and uniform warming (dark red) simulations. (d) Atlantic meridional overturning circulation: integrated meridional transport for $\sigma_2 \in [1035.5, 1038.0] \text{ kg m}^{-3}$ at 26°N for longitudes between 103°W and 5°W . (e) Antarctic Circumpolar Current transport through the Drake Passage. (f) Globally integrated kinetic energy.

Over time, the lateral buoyancy gradients become less proportional to the surface buoyancy flux perturbations (compare Figs. 5c and f; Figs. 6c and f; Figs. 10c and f; Figs. 11c and f). A divergence from this linear relationship with time could be attributed to several factors such as lateral variations in mixed layer depth (Xie et al. 2010) and advective feedbacks between the surface buoyancy forcing anomalies and the ocean circulation (Bryden et al. 1991). For example, in the -15 W m^{-2} simulation, this non-linear connection can be most clearly observed in the spin-up of the North Atlantic subtropical gyre in the last 20 years (Fig. 4a) and a surge in the AMOC in the last 40 years (Fig. 7a). The ocean circulation in the increased surface buoyancy flux contrast simulations is more non-linearly related to surface buoyancy flux gradient perturbation than the reduced surface buoyancy flux contrast simulations. For example, we observe a slowdown in North

Atlantic, South Atlantic, and South Pacific gyre strength in the last 40 years of the $+15 \text{ W m}^{-2}$ simulation (Fig. 8) and an oscillatory AMOC in both $+7.5 \text{ W m}^{-2}$ and $+15 \text{ W m}^{-2}$ simulations (Fig. 12a).

The flux-forced simulations allowed us to conduct perturbation simulations in which each surface forcing could be altered independently. However, the present study has numerous caveats. Firstly, in reality the wind and buoyancy forcing are strongly coupled. In earlier experiments that used bulk formula for the surface heat fluxes (not shown), we found that decreasing the wind forcing strongly reduced the surface buoyancy fluxes as well due to the reduction in poleward heat transport. Next, the flux-forced simulations are conducted at 0.25° resolution and can only partially capture the mesoscale eddies. Moreover, the flux-forced control simulation is not fully equilibrated (see Fig. 1c) due to the dynamic frazil formation at high latitudes, which

continuously adds heat in the polar regions. The frazil formation limits the magnitude of surface buoyancy flux perturbation we can apply in the polar regions. We have partially muted the frazil heat gain in the increased surface buoyancy flux contrast experiments through adding a globally uniform heat loss. In regions of extreme buoyancy anomalies, the isopycnal outcropping method (section 2b) is prone to capturing other elements of ocean circulation especially in regions of heat gain, such as the deep cell of the AMOC, which may produce erroneous results. Finally, the surface buoyancy flux perturbation experiments have not equilibrated even after 100 years, and hence, should not be misunderstood as the final response.

The present study reinforces recent evidence supporting the existence of a buoyancy-driven component in ocean gyres (Gjermundsen et al. 2018; Hogg and Gayen 2020; Liu et al. 2022). We envisage that a complete theory describing the formation of ocean gyres should incorporate the effects of surface buoyancy forcing, in addition to surface wind stress (Munk 1950). However, the influence of surface buoyancy forcing on gyres depends on the ocean state, allowing non-linear and non-local feedbacks with the ocean circulation that obscure the formulation of a simple theory. These feedbacks may include the role of the mixed layer in capturing excess heat and the horizontal transport of heat by the circulation, both of which influence the background stratification.

Acknowledgments. We would like to thank the community of the Consortium for Ocean–Sea Ice Modeling in Australia (<http://cosima.org.au>) for helpful discussions and for the development and maintenance of cosima-cookbook package (<https://github.com/COSIMA/cosima-cookbook>) and the cosima-recipes repository (<https://github.com/COSIMA/cosima-recipes>), both of which are indispensable for our workflow. D.B. would like to thank Bishakhdatta Gayen, Aviv Solodoch, Andy Thompson, and Christopher Wolfe for stimulating discussions during early stages of this work. D.B. expresses gratitude to the Computational Modeling Systems group at the Australian Research Council Center for Climate Extremes for their assistance in conducting the flux-forced simulations. Our analyses were facilitated with the Python packages `dask` (Rocklin 2015) and `xarray` (Hoyer and Hamman 2017). Computational resources were provided by the Australian National Computational Infrastructure at the ANU, which is supported by the Commonwealth Government of Australia. R.M.H. is supported by the Australian Research Council DECRA Fellowship DE210100004. N.C.C. is supported by the Australian Research Council DECRA Fellowship DE210100749.

Data availability statement. Python code used for generating figures are available at <https://github.com/dhruvbjagtani/varying-surface-forcing>. Output

to reproduce figures will be available in a Zenodo repository upon acceptance of manuscript. MOM5 source code for flux-forced simulations is available at <https://github.com/dhruvbjagtani/MOM5>.

APPENDIX

K-profile ocean surface boundary layer parameterization

The ACCESS-OM2 control and flux-forced simulations estimate the mixing layer depth using the K-profile parameterization (Large et al. 1994). The mixing layer depth depends on many factors, such as Langmuir turbulence (Belcher et al. 2012), surface buoyancy forcing (Yoshikawa 2015), wind stress (Grant and Belcher 2011), and convection (Sohail et al. 2020). The effect of these processes on the mixing layer depth can be encapsulated in the Richardson number, which is the ratio of stratification, $\partial_z b$, and vertical flow shear squared, $|\partial_z u|^2$. The K-profile parameterization uses the bulk Richardson number Ri_b (Stull 1988) defined over a depth h :

$$Ri_b(h) = \frac{[b(0) - b(-h)]/h}{|\mathbf{u}(0) - \mathbf{u}(-h)|^2/h^2 + u_{\text{turb}}^2/h^2}, \quad (\text{A1})$$

where, e.g., $b(-h) \equiv b(x, y, z = -h, t)$. In (A1), the numerator is the mean stratification averaged over depth h and in the denominator, $|\mathbf{u}(0) - \mathbf{u}(-h)|/h$ is the magnitude of the resolved velocity shear averaged over depth h while term u_{turb}/h quantifies the unresolved/turbulent velocity shear. The parameterization determines the mixing layer depth h such that $Ri_b(h)$ is equal to a critical Richardson number, typically taken to be 0.25–0.3.

Prior to creating the flux-forced simulations, we conducted wind sensitivity experiments using ACCESS-OM2-025 (not presented here) along with the traditional K-profile parameterization reported in Large et al. (1994). However, the surface buoyancy forcing was inadvertently modified in these sensitivity experiments through anomalies in the mixing layer depth and ocean circulation. In an attempt to minimize surface buoyancy flux variations in the ACCESS-OM2-025 wind stress sensitivity experiments, we reconstructed the resolved velocity shear term $|\mathbf{u}(0) - \mathbf{u}(-h)|/h$ in (A1) in the K-profile parameterization, which was found to primarily cause mixing layer depth anomalies in the sensitivity experiments. We parameterized $|\mathbf{u}(0) - \mathbf{u}(-h)|$ as a function of the friction velocity, $u_* = (|\boldsymbol{\tau}|/\rho_0)^{1/2}$ and depth h :

$$|\mathbf{u}(0) - \mathbf{u}(-h)|^2 = (c_a u_*^2 + c_b u_*)(1 - e^{-c_e h/\sqrt{u_*}}), \quad (\text{A2})$$

where c_a , c_b , and c_e were coefficients found using multivariate linear regression. Table A1 lists typical ranges of the three parameters for an optimal solution. The parameterization (A2) performs well in the tropical and subtropical

regions. Errors in the polar regions are expected because our parameterization (A2) does not account for sea ice and marginal ice zone so as to stay consistent with the flux-forced experiments, which could alter resolved velocity shear in these regions.

TABLE A1: Ranges of parameters for resolved velocity shear obtained using multi-variate linear-regression.

Coefficient	Range
c_a	50–70
c_b	0.8–1.2 m s ⁻¹
c_e	0.009–0.011 (m s) ^{-1/2}

The parameterization prevented discrepancies in the mixing layer depth due to alterations in the wind stress, and was implemented in the ACCESS-OM2-025 control experiment (Fig. 1c). To maintain consistency with the ACCESS-OM2-025 control simulation, we retained the resolved shear parameterization in the flux-forced simulations.

References

- Abernathy, R., and D. Ferreira, 2015: Southern Ocean isopycnal mixing and ventilation changes driven by winds. *Geophysical Research Letters*, **42**, 10 357–10 365, <https://doi.org/10.1002/2015GL066238>.
- Abernathy, R. P., A. Gnanadesikan, M.-A. Pradal, and M. A. Sundermeyer, 2022: Chapter 9 - Isopycnal mixing. *Ocean Mixing*, M. Meredith, and A. Naveira Garabato, Eds., Elsevier, 215–256, <https://doi.org/10.1016/B978-0-12-821512-8.00016-5>.
- Anderson, D. L., and A. E. Gill, 1975: Spin-up of a stratified ocean, with applications to upwelling. *Deep-Sea Research and Oceanographic Abstracts*, **22**, 583–596, [https://doi.org/10.1016/0011-7471\(75\)90046-7](https://doi.org/10.1016/0011-7471(75)90046-7).
- Belcher, S. E., and Coauthors, 2012: A global perspective on Langmuir turbulence in the ocean surface boundary layer. *Geophysical Research Letters*, **39**, 1–9, <https://doi.org/10.1029/2012GL052932>.
- Berglund, S., K. Döös, S. Groeskamp, and T. J. McDougall, 2022: The downward spiralling nature of the North Atlantic subtropical gyre. *Nature Communications*, **13**, 1–9, <https://doi.org/10.1038/s41467-022-29607-8>.
- Bryden, H. L., D. H. Roemmich, and J. A. Church, 1991: Ocean heat transport across 24°N in the Pacific. *Deep Sea Research Part A, Oceanographic Research Papers*, **38**, [https://doi.org/10.1016/0198-0149\(91\)90070-V](https://doi.org/10.1016/0198-0149(91)90070-V).
- Chen, C., G. Wang, S. P. Xie, and W. Liu, 2019: Why does global warming weaken the Gulf Stream but intensify the Kuroshio? *Journal of Climate*, **32**, 7437–7451, <https://doi.org/10.1175/JCLI-D-18-0895.1>.
- Cheng, W., J. C. Chiang, and D. Zhang, 2013: Atlantic Meridional Overturning Circulation (AMOC) in CMIP5 models: RCP and historical simulations. *Journal of Climate*, **26**, 7187–7197, <https://doi.org/10.1175/JCLI-D-12-00496.1>.
- Colin de Verdière, A., 1989: On the interaction of wind and buoyancy driven gyres. *Journal of Marine Research*, **47**, 595–633, <https://doi.org/10.1357/00222408978507172>.
- Colin De Verdière, A., and M. Ollitrault, 2016: A direct determination of the world ocean barotropic circulation. *Journal of Physical Oceanography*, **46**, 255–273, <https://doi.org/10.1175/JPO-D-15-0046.1>.
- Constantinou, N. C., and A. M. C. Hogg, 2019: Eddy saturation of the Southern Ocean: A baroclinic versus barotropic perspective. *Geophysical Research Letters*, **46**, 12 202–12 212, <https://doi.org/10.1029/2019GL084117>.
- Cox, M. D., and K. Bryan, 1984: A numerical model of the ventilated thermocline. *Journal of Physical Oceanography*, **14**, 674–687, [https://doi.org/10.1175/1520-0485\(1984\)014<0674:anmotv>2.0.co;2](https://doi.org/10.1175/1520-0485(1984)014<0674:anmotv>2.0.co;2).
- Drake, H. F., R. Ferrari, and J. Callies, 2020: Abyssal circulation driven by near-boundary mixing: Water mass transformations and interior stratification. *Journal of Physical Oceanography*, **50**, 2203–2226, <https://doi.org/10.1175/JPO-D-19-0313.1>.
- Gayen, B., and R. W. Griffiths, 2021: Rotating horizontal convection. *Annual Review of Fluid Mechanics*, **54**, 105–132, <https://doi.org/10.1146/annurev-fluid-030121-115729>.
- Gent, P. R., and J. C. McWilliams, 1990: Isopycnal mixing in ocean circulation models. *Journal of Physical Oceanography*, **20**, 150–155, [https://doi.org/10.1175/1520-0485\(1990\)020<0150:IMIOCM>2.0.CO;2](https://doi.org/10.1175/1520-0485(1990)020<0150:IMIOCM>2.0.CO;2).
- Gjermundsen, A., J. H. Lacasce, and L. Denstad, 2018: The thermally driven ocean circulation with realistic bathymetry. *Journal of Physical Oceanography*, **48**, 647–665, <https://doi.org/10.1175/JPO-D-17-0147.1>.
- Goldsbrough, G. R., 1933: Ocean currents produced by evaporation and precipitation. *Proceedings of the Royal Society of London. Series A, Containing Papers of a Mathematical and Physical Character*, **141**, 512–517, <https://doi.org/10.1098/rspa.1933.0135>.
- Grant, A. L. M., and S. E. Belcher, 2011: Wind-driven mixing below the oceanic mixed layer. *Journal of Physical Oceanography*, **41**, 1556–1575, <https://doi.org/10.1175/JPO-D-10-05020.1>.
- Gray, A. R., and S. C. Riser, 2014: A global analysis of Sverdrup balance using absolute geostrophic velocities from Argo. *Journal of Physical Oceanography*, **44**, 1213–1229, <https://doi.org/10.1175/JPO-D-12-0206.1>.
- Griffies, S. M., 2012: Elements of the Modular Ocean Model (MOM) 2012 release with updates. URL www.gfdl.noaa.gov/fms.
- Hazeleger, W., and S. Drijfhout, 2006: Subtropical cells and Meridional Overturning Circulation pathways in the tropical Atlantic. *Journal of Geophysical Research: Oceans*, **111**, 1–13, <https://doi.org/10.1029/2005JC002942>.
- Hogg, A. M., 2010: An Antarctic Circumpolar Current driven by surface buoyancy forcing. *Geophysical Research Letters*, **37**, 1–5, <https://doi.org/10.1029/2010GL044777>.
- Hogg, A. M., P. Spence, O. A. Saenko, and S. M. Downes, 2017: The energetics of Southern Ocean upwelling. *Journal of Physical Oceanography*, **47**, 135–153, <https://doi.org/10.1175/JPO-D-16-0176.1>.
- Hogg, A. M. C., and B. Gayen, 2020: Ocean gyres driven by surface buoyancy forcing. *Geophysical Research Letters*, **47**, 1–10, <https://doi.org/10.1029/2020GL088539>.

- Hoyer, S., and J. Hamman, 2017: xarray: N-D labeled arrays and datasets in Python. *Journal of Open Research Software*, **5**, 1–10, <https://doi.org/10.5334/jors.148>.
- Hughes, C. W., and B. A. D. Cuevas, 2001: Why western boundary currents in realistic oceans are inviscid: A link between form stress and bottom pressure torques. *Journal of Physical Oceanography*, **31**, 2871–2885, [https://doi.org/10.1175/1520-0485\(2001\)031<2871:WWBCIR>2.0.CO;2](https://doi.org/10.1175/1520-0485(2001)031<2871:WWBCIR>2.0.CO;2).
- Hughes, C. W., and C. Wilson, 2008: Wind work on the geostrophic ocean circulation: An observational study of the effect of small scales in the wind stress. *Journal of Geophysical Research: Oceans*, **113**, 1–10, <https://doi.org/10.1029/2007JC004371>.
- Hughes, G. O., A. M. Hogg, and R. W. Griffiths, 2009: Available potential energy and irreversible mixing in the Meridional Overturning Circulation. *Journal of Physical Oceanography*, **39**, 3130–3146, <https://doi.org/10.1175/2009JPO4162.1>.
- Hunke, E. C., W. H. Lipscomb, A. K. Turner, N. Jeffery, and S. Elliott, 2015: CICE: the Los Alamos Sea Ice Model documentation and software user's manual version 5.1 la-cc-06-012. URL <https://github.com/CICE-Consortium/CICE/wiki>.
- Jamet, Q., B. Deremble, N. Wienders, T. Uchida, and W. K. Dewar, 2021: On wind-driven energetics of subtropical gyres. *Journal of Advances in Modeling Earth Systems*, **13**, 1–23, <https://doi.org/10.1029/2020MS002329>.
- Kiss, A. E., and Coauthors, 2020: ACCESS-OM2 v1.0: a global ocean-sea ice model at three resolutions. *Geoscientific Model Development*, **13**, 401–442, <https://doi.org/10.5194/gmd-13-401-2020>.
- Klockmann, M., U. Mikolajewicz, H. Kleppin, and J. Marotzke, 2020: Coupling of the subpolar gyre and the overturning circulation during abrupt glacial climate transitions. *Geophysical Research Letters*, **47**, 1–11, <https://doi.org/10.1029/2020GL090361>.
- Large, W. G., J. C. McWilliams, and S. C. Doney, 1994: Oceanic vertical mixing: A review and a model with a nonlocal boundary layer parameterization. *Reviews of Geophysics*, **32** (4), 363–403, <https://doi.org/10.1029/94RG01872>.
- Large, W. G., and S. G. Yeager, 2009: The global climatology of an interannually varying air - sea flux data set. *Climate Dynamics*, **33**, <https://doi.org/10.1007/s00382-008-0441-3>.
- Larson, S. M., M. W. Buckley, and A. C. Clement, 2020: Extracting the buoyancy-driven Atlantic Meridional Overturning Circulation. *Journal of Climate*, **33**, 4697–4714, <https://doi.org/10.1175/JCLI-D-19-0590.1>.
- Lavergne, C. D., S. Groeskamp, J. Zika, and H. L. Johnson, 2021: The role of mixing in the large-scale ocean circulation. Elsevier, 35–63 pp., <https://doi.org/10.1016/B978-0-12-821512-8.00010-4>.
- Li, J., M. Roughan, and C. Kerry, 2022: Drivers of ocean warming in the western boundary currents of the Southern Hemisphere. *Nature Climate Change*, **12**, 901–909, <https://doi.org/10.1038/s41558-022-01473-8>.
- Liu, T., H. W. Ou, X. Liu, Y. K. Qian, and D. Chen, 2022: The dependence of upper ocean gyres on wind and buoyancy forcing. *Geoscience Letters*, **9**, 1–8, <https://doi.org/10.1186/s40562-022-00213-2>.
- Locarnini, R. A., A. V. Mishonov, J. I. Antonov, T. P. Boyer, H. E. Garcia, O. K. Baranova, M. M. Zweng, and D. R. Johnson, 2010: World Ocean Atlas 2009, vol. 1. *Temperature, NOAA Atlas NESDIS*, **68**.
- Locarnini, R. A., and Coauthors, 2013: World Ocean Atlas 2013. vol. 1: Temperature. 1–48 pp.
- Lohmann, G., H. Haak, and J. H. Jungclaus, 2008: Estimating trends of Atlantic Meridional Overturning Circulation from long-term hydrographic data and model simulations. *Ocean Dynamics*, **58**, 127–138, <https://doi.org/10.1007/s10236-008-0136-7>.
- Lohmann, K., D. A. Putrasahan, J. S. von Storch, O. Gutjahr, J. H. Jungclaus, and H. Haak, 2021: Response of northern North Atlantic and Atlantic Meridional Overturning Circulation to reduced and enhanced wind stress forcing. *Journal of Geophysical Research: Oceans*, **126**, 1–22, <https://doi.org/10.1029/2021JC017902>.
- Luyten, J., H. Stommel, and C. Wunsch, 1985: A diagnostic study of the northern Atlantic subpolar gyre. *Journal of Physical Oceanography*, **15**, 1344–1348, [https://doi.org/10.1175/1520-0485\(1985\)015<1344:adsotn>2.0.co;2](https://doi.org/10.1175/1520-0485(1985)015<1344:adsotn>2.0.co;2).
- Luyten, J. R., J. Pedlosky, and H. Stommel, 1983: The ventilated thermocline. *Journal of Physical Oceanography*, **13**, 292–309, [https://doi.org/10.1175/1520-0485\(1983\)013<0292:TVC>2.0.CO;2](https://doi.org/10.1175/1520-0485(1983)013<0292:TVC>2.0.CO;2).
- Marshall, D. P., M. H. Ambaum, J. R. Maddison, D. R. Munday, and L. Novak, 2017: Eddy saturation and frictional control of the Antarctic Circumpolar Current. *Geophysical Research Letters*, **44**, 286–292, <https://doi.org/10.1002/2016GL071702>.
- Marshall, J., and K. Speer, 2012: Closure of the Meridional Overturning Circulation through Southern Ocean upwelling. *Nature Geoscience*, **5**, 171–180, <https://doi.org/10.1038/ngeo1391>.
- McDowell, S., P. Rhines, and T. Keffer, 1982: North Atlantic potential vorticity and its relation to the general circulation. *Journal of Physical Oceanography*, **12**, 1417–1436, [https://doi.org/10.1175/1520-0485\(1982\)012<1417:napvai>2.0.co;2](https://doi.org/10.1175/1520-0485(1982)012<1417:napvai>2.0.co;2).
- Morrison, A. K., A. M. Hogg, and M. L. Ward, 2011: Sensitivity of the Southern Ocean overturning circulation to surface buoyancy forcing. *Geophysical Research Letters*, **38**, 1–5, <https://doi.org/10.1029/2011GL048031>.
- Morrison, A. K., and A. M. C. Hogg, 2013: On the relationship between Southern Ocean overturning and ACC transport. *Journal of Physical Oceanography*, **43**, 140–148, <https://doi.org/10.1175/JPO-D-12-057.1>.
- Munday, D. R., H. L. Johnson, and D. P. Marshall, 2013: Eddy saturation of equilibrated circumpolar currents. *Journal of Physical Oceanography*, **43**, 507–532, <https://doi.org/10.1175/JPO-D-12-095.1>.
- Munk, W. H., 1950: On the wind-driven ocean circulation. *Journal of Meteorology*, **7**, 80–93, [https://doi.org/10.1175/1520-0469\(1950\)007<0080:OTWDOC>2.0.CO;2](https://doi.org/10.1175/1520-0469(1950)007<0080:OTWDOC>2.0.CO;2).
- Oka, A., and Y. Niwa, 2013: Pacific deep circulation and ventilation controlled by tidal mixing away from the sea bottom. *Nature Communications*, **4**, 1–8, <https://doi.org/10.1038/ncomms3419>.
- Ollitrault, M., and J. P. Rannou, 2013: ANDRO: An Argo-based deep displacement dataset. *Journal of Atmospheric and Oceanic Technology*, **30**, 759–788, <https://doi.org/10.1175/JTECH-D-12-00073.1>.
- Palter, J. B., 2015: The role of the Gulf Stream in European climate. *Annual Review of Marine Science*, **7**, 113–137, <https://doi.org/10.1146/annurev-marine-010814-015656>.

- Pedlosky, J., 1986: The buoyancy and wind-driven ventilated thermocline. *Journal of Physical Oceanography*, **16**, 1077–1087, [https://doi.org/10.1175/1520-0485\(1986\)016<1077:TBAWDV>2.0.CO;2](https://doi.org/10.1175/1520-0485(1986)016<1077:TBAWDV>2.0.CO;2).
- Ragen, S., M. A. Pradal, and A. Gnanadesikan, 2020: The impact of parameterized lateral mixing on the Antarctic Circumpolar Current in a coupled climate model. *Journal of Physical Oceanography*, **50**, 965–982, <https://doi.org/10.1175/JPO-D-19-0249.1>.
- Rhines, P. B., and W. R. Young, 1982: Homogenization of potential vorticity in planetary gyres. *Journal of Fluid Mechanics*, **122**, 347–367, <https://doi.org/10.1017/S0022112082002250>.
- Rocklin, M., 2015: Dask: Parallel computation with blocked algorithms and task scheduling. *Proceedings of the 14th Python in Science Conference*, K. Huff, and J. Bergstra, Eds., 126–132, <https://doi.org/10.25080/Majora-7b98e3ed-013>.
- Roemmich, D., S. Riser, R. Davis, and Y. Desaubies, 2004: Autonomous profiling floats: Workhorse for broad-scale ocean observations. *Marine Technology Society Journal*, **38**, 21–29, <https://doi.org/10.4031/002533204787522802>.
- Saenko, O. A., 2009: On the climatic impact of wind stress. *Journal of Physical Oceanography*, **39**, 89–106, <https://doi.org/10.1175/2008JPO3981.1>.
- Sakamoto, T. T., H. Hasumi, M. Ishii, S. Emori, T. Suzuki, T. Nishimura, and A. Sumi, 2005: Responses of the Kuroshio and the Kuroshio extension to global warming in a high-resolution climate model. *Geophysical Research Letters*, **32**, 1–4, <https://doi.org/10.1029/2005GL023384>.
- Shi, J. R., L. D. Talley, S. P. Xie, W. Liu, and S. T. Gille, 2020: Effects of buoyancy and wind forcing on Southern Ocean climate change. *Journal of Climate*, **33**, 10 003–10 020, <https://doi.org/10.1175/JCLI-D-19-0877.1>.
- Sohail, T., B. Gayen, and A. M. Hogg, 2020: The dynamics of mixed layer deepening during open-ocean convection. *Journal of Physical Oceanography*, **50**, 1625–1641, <https://doi.org/10.1175/JPO-D-19-0264.1>.
- Stanley, G. J., and O. A. Saenko, 2014: Bottom-enhanced diapycnal mixing driven by mesoscale eddies: Sensitivity to wind energy supply. *Journal of Physical Oceanography*, **44**, 68–85, <https://doi.org/10.1175/JPO-D-13-0116.1>.
- Stewart, K., and Coauthors, 2020: JRA55-do-based repeat year forcing datasets for driving ocean–sea-ice models. *Ocean Modelling*, **147**, 1–27, <https://doi.org/10.1016/j.ocemod.2019.101557>.
- Stommel, H., 1948: The westward intensification of wind-driven ocean currents. *Transactions, American Geophysical Union*, **29**, 202–206, <https://doi.org/10.1029/TR029i002p00202>.
- Stommel, H., 1961: Thermohaline convection with two stable regimes of flow. *Tellus*, **13**, 224–230, <https://doi.org/10.1111/j.2153-3490.1961.tb00079.x>.
- Stommel, H., and A. B. Arons, 1959: On the abyssal circulation of the world ocean-I. Stationary planetary flow patterns on a sphere. *Deep Sea Research (1953)*, **6**, 217–233, [https://doi.org/10.1016/0146-6313\(59\)90065-6](https://doi.org/10.1016/0146-6313(59)90065-6).
- Stull, R. B., 1988: *An introduction to boundary layer meteorology*. 1–670 pp., <https://doi.org/10.1007/978-94-009-3027-8>.
- Sverdrup, H. U., 1947: Wind-driven currents in a baroclinic ocean; with application to the equatorial currents of the eastern Pacific. *Proceedings of the National Academy of Sciences*, **33**, 318–326, <https://doi.org/10.1073/pnas.33.11.318>.
- Tailleux, R., 2009: On the energetics of stratified turbulent mixing, irreversible thermodynamics, Boussinesq models and the ocean heat engine controversy. *Journal of Fluid Mechanics*, **638**, 339–382, <https://doi.org/10.1017/S002211200999111X>.
- Talley, L. D., G. L. Pickard, W. J. Emery, and J. H. Swift, 2011: *Descriptive physical oceanography: An introduction: Sixth edition*. Academic Press, 1–555 pp., <https://doi.org/10.1016/C2009-0-24322-4>.
- Toggweiler, J. R., and B. Samuels, 1995: Effect of Drake Passage on the global thermohaline circulation. *Deep-Sea Research Part I*, **42**, 477–500, [https://doi.org/10.1016/0967-0637\(95\)00012-U](https://doi.org/10.1016/0967-0637(95)00012-U).
- Tsujino, H., and Coauthors, 2018: JRA55 based surface dataset for driving ocean–sea-ice models (JRA55-do). *Ocean Modelling*, **130**, 79–139, <https://doi.org/10.1016/j.ocemod.2018.07.002>.
- Veronis, G., and H. Stommel, 1956: The action of variable wind stresses on a stratified ocean. *Journal of Marine Research*, **15**, 43–75.
- Webb, P., 2017: *Introduction to oceanography*. Online OER Textbook, Roger Williams University, URL <https://pressbooks.pub/webboceanography1/>.
- Wunsch, C., and R. Ferrari, 2004: Vertical mixing, energy, and the general circulation of the oceans. *Annual Review of Fluid Mechanics*, **36**, 281–314, <https://doi.org/10.1146/annurev.fluid.36.050802.122121>.
- Xie, S. P., C. Deser, G. A. Vecchi, J. Ma, H. Teng, and A. T. Wittenberg, 2010: Global warming pattern formation: Sea surface temperature and rainfall. *Journal of Climate*, **23**, 966–986, <https://doi.org/10.1175/2009JCLI3329.1>.
- Yang, H., K. Wang, H. Dai, Y. Wang, and Q. Li, 2016: Wind effect on the Atlantic Meridional Overturning Circulation via sea ice and vertical diffusion. *Climate Dynamics*, **46**, 3387–3403, <https://doi.org/10.1007/s00382-015-2774-z>.
- Yeager, S., 2015: Topographic coupling of the Atlantic overturning and gyre circulations. *Journal of Physical Oceanography*, **45**, 1258–1284, <https://doi.org/10.1175/JPO-D-14-0100.1>.
- Yeager, S., and G. Danabasoglu, 2014: The origins of late-twentieth-century variations in the large-scale North Atlantic circulation. *Journal of Climate*, **27**, 3222–3247, <https://doi.org/10.1175/JCLI-D-13-00125.1>.
- Yoshikawa, Y., 2015: Scaling surface mixing/mixed layer depth under stabilizing buoyancy flux. *Journal of Physical Oceanography*, **45**, 247–258, <https://doi.org/10.1175/JPO-D-13-0190.1>.
- Zhang, Y., X. Zheng, D. Kong, H. Yan, and Z. Liu, 2021: Enhanced North Pacific subtropical gyre circulation during the late Holocene. *Nature Communications*, **12**, 1–10, <https://doi.org/10.1038/s41467-021-26218-7>.
- Zweng, M. M., and Coauthors, 2013: World Ocean Atlas 2013, volume 2: Salinity. 1–47 pp.